

ARMY RESEARCH LABORATORY



Determination of the Yield Strength of a Molybdenum Jet

by Miles L. Lampson
and Richard L. Summers

ARL-TR-1639

March 1998

19980417 005

2025 RELEASE UNDER E.O. 14176

DTIC QUALITY LINE 228

Approved for public release; distribution is unlimited.

The findings in this report are not to be construed as an official Department of the Army position unless so designated by other authorized documents.

Citation of manufacturer's or trade names does not constitute an official endorsement or approval of the use thereof.

Destroy this report when it is no longer needed. Do not return it to the originator.

Abstract

The strength of the metal in a shaped charge jet influences its length at breakup, its penetration rate into a target, and its ability to resist aerodynamic forces in flight. The response of a jet to an imposed centrifugal force can be used to estimate its yield strength. Copper was the first metal studied by this technique, and the strength determined by Karpp using a hoop model was approximately 100 MPa. We have studied molybdenum using the same experimental technique and analyzed the data using a hoop, a disk, and a cylinder model of the jet. The yield strength and its associated uncertainty were estimated from the observed kinematics of the portion of the jet fragmented by the centrifugal force and the computed jet spin rate.

Acknowledgments

The authors would like to express their thanks to Mr. Carl Paxton and Mr. Joseph Gardiner, who conducted these experiments; to Mr. Gary Sprenkle, who fabricated the hardware; and to Mr. Raymond Cregar and Mr. William Gault, who cast the explosive fills.

INTENTIONALLY LEFT BLANK.

Table of Contents

	<u>Page</u>
Acknowledgments	iii
List of Figures	vii
List of Tables	ix
1. Introduction	1
2. The Models	3
3. Experiments	5
4. Jet Measurements	6
5. Strength Estimates From Radiographic Measurements	10
6. Strength Estimates From Calculations and Radiographic Data	12
7. Discussion	20
8. Conclusion	22
9. References	23
Appendix A: Stresses in Solid and Annular Disks	25
Appendix B: Stresses in Solid and Annular Cylinders	43
Appendix C: Computed Jet Characteristics	57
Distribution List	67
Report Documentation Page	71

INTENTIONALLY LEFT BLANK.

List of Figures

<u>Figure</u>	<u>Page</u>
1. Schematic Diagram of a Shaped Charge Device	6
2. Flash Radiograph of Nonrotating Jet Pellet Taken at $t = 180 \mu s$	7
3. Flash Radiograph of Nonrotating Jet Pellet Taken at $t = 936 \mu s$	7
4. Flash Radiograph of Pellet From Device Spinning at 42 rps Taken at $140 \mu s$	8
5. Flash Radiograph of Pellet From Device Spinning at 42 rps Taken at $220 \mu s$	9
6. Flash Radiograph of Pellet From Device Spinning at 60 rps Taken at $160 \mu s$	9
7. Flash Radiograph of Pellet From Device Spinning at 60 rps Taken at $200 \mu s$	10
8. Calculated Jet Velocity as a Function of Position Along the Liner and Computed Pellet Shape	14
9. Collapse Sequence Computed for Liner Element 5 and Resulting Jet Element ...	15
10. Calculated As-Formed Spin Rate of Jet as a Function of Position Along the Liner and Initial Liner Spin Rate	16
A-1. Scaled Stresses and Displacements of the Spinning Solid Disk at the Critical Velocity	34
A-2. Scaled Stresses in the Fully Plastic Spinning Solid Disk	36
A-3. Scaled Stresses in the Spinning Annular Disk at the Critical Velocity	38
A-4. Scaled Stresses in the Fully Plastic Spinning Annular Disk	41
B-1. Scaled Stresses in the Fully Plastic Spinning Annular Cylinder	56

INTENTIONALLY LEFT BLANK.

List of Tables

<u>Table</u>		<u>Page</u>
1. Experimental Data		11
2. Computed Radii and Angular Velocities of Elements 61-71		17
C-1. Computed Jet Properties		62
C-2. Comparison of the Models for Liner Element 64		65

INTENTIONALLY LEFT BLANK.

1. Introduction

The strength of the metal in a shaped charge jet influences the length of the jet at breakup (Walsh 1984), its penetration rate into a target (Eichelberger 1956), and its response to aerodynamic forces in flight. It may also be of interest to those devising constitutive equations for metals experiencing large, rapid deformations.

In the early 1970s, Karpp and Simon (1976) devised a method to estimate the strength of a jet from the angular velocity at which it was observed to burst radially. In their experiments, a copper-lined shaped charge was detonated while spinning about its axis of symmetry, creating a jet with a range of spin rates. Due to the conservation of angular momentum, the jet spin rates are much higher than the spin rate of the shaped charge. Using sequential flash radiographs of these spinning copper jets, the width of the pattern formed by the radially expanding jet fragments, D , was measured at the various flash times. From this information and the assumption that the cross section of the jet resembles a tube, the angular velocity of the pellet when it was intact, ω , was approximated by the relation

$$\omega = \frac{V}{r} = \frac{1}{2r} \frac{dD}{dt}, \quad (1)$$

where r is the average radius to the centroid of the fragmented pellet, V is the tangential velocity at the centroid, and $\frac{dD}{dt}$ is the diametrical expansion rate of the fragment pattern. If the jet pellet next to one that burst remains intact and is assumed to have the critical value of angular velocity that just causes yielding, ω_f , then ω_f is approximately equal to the measured ω and the yield strength, σ_o , is given by

$$\sigma_o = \rho r^2 \omega_f^2, \quad (2)$$

where ρ is the density of the jet. In this stress equation, the jet is modeled as a hoop. A yield strength of 100 MPa was determined for copper using this technique.

In this report, a molybdenum jet is studied using the same experimental technique. The charge configuration used differed from the one used in the Karpp-Simon experiments. This shaped charge produced a jet with a different shape and it was not possible to determine whether the jet was solid or hollow, so the effect of using different geometric models of the jet to evaluate the yield strength was investigated. The stress formulas corresponding to these geometries are given in section 2.

Sections 3 and 4 describe the experimental hardware and the measurements taken from the radiographs.

In section 5, attempts are made to infer the geometry of the jet from the dimensions of the burst fragments. Yield strengths corresponding to the experimental measurements and the possible geometries are computed, and an estimate is made of the uncertainty. Since the experiments only provide an estimate of angular velocity for a jet element that bursts, the actual stress required to cause bursting must be less than the stress calculated from the experimental data.

The Karpp-Simon equation for estimating ω from radiographic data will underestimate the angular velocity in cases in which the jet bursts into only a few fragments, because the sparsely defined diameter of the pattern will be underestimated. However, the angular velocity may also be estimated from a jet-formation calculation, and this method is used to cross-check ω . The calculation can also provide the spin rate for the neighboring jet element that does not burst and, hence, a lower limit for the yield strength. The procedure for obtaining the yield strength from the calculations and the radiographic measurements is discussed in section 6.

The yield strengths determined in sections 5 and 6 are discussed in section 7 of the report. Section 8 gives the conclusions.

2. The Models

After the jet has formed, attention is focused on the element spinning at the critical spin rate that just causes yielding. For analytic tractability, the jet segment is assumed to decouple from its neighbors (i.e., break axially) before it can fail under the centrifugal force. Thus, the spinning jet is modeled in the same manner as used to determine the maximum rate of rotation a flywheel can withstand without bursting radially. The material is assumed to be homogeneous, isotropic, and perfectly plastic. In addition, bursting is assumed to occur when the spin rate reaches a level that causes the entire jet cross section to reach the Tresca yield criterion. For a given critical spin rate, the value inferred for the strength depends on the geometry used to represent the jet. The state of stress can be computed by treating the segment as a thin disk (plane stress), using a formula derived in Appendix A (equation A-50), or as a long cylinder (plane strain), using formulas derived in Appendix B. For an annular disk, the yield strength in simple tension, σ_o , is related to the angular velocity at failure, ω_f , by the relation

$$\sigma_o = \frac{\rho \omega_f^2 (r_o^2 + r_o r_i + r_i^2)}{3} , \quad (3)$$

where ρ is the mass density, r_i is the inner radius, and r_o is the outer radius. In the limit in which r_i approaches r_o , the hoop form used by Karpp, equation 2, is obtained. If $r_i = 0$ in equation 3, one gets the result for a solid disk (Nadai 1950):

$$\sigma_o = \frac{\rho r_o^2 \omega_f^2}{3} . \quad (4)$$

In the case of a solid cylinder, the yield strength is given by

$$\sigma_o = \frac{\rho r_o^2 \omega_f^2}{4} - \frac{T}{\pi r_o^2} , \quad (5)$$

where T is the net axial force acting on the cylinder. Since σ_o is a constant, for a given angular velocity the cylinder may be in equilibrium while under a positive axial force (tension) and fail when the tension is relieved. The case of the hollow cylinder must be solved numerically (Davis and Connelly 1959); however, the results for the freely rotating annular cylinder (with no axial force) are similar to those of the analytic annular disk under most conditions.

In order to compute the spin rate of the jet at burst using equation 1, the average radius to the centroid of the fragments, r_c , or its equivalent, must be estimated. In this study, it is assumed that the jet bursts symmetrically, and so the radial distance to the center of mass of the fragment, r_c , replaces r . If the jet is solid with an outer radius r_o and breaks symmetrically into n fragments, then

$$r_c = kr_o, \quad (6)$$

where, since each fragment subtends an angle $2\pi/n$,

$$k = \frac{2}{3} \frac{\sin(\pi/n)}{\pi/n}. \quad (7)$$

If the jet is hollow, then

$$r_c = k \frac{(r_o^3 - r_i^3)}{(r_o^2 - r_i^2)}. \quad (8)$$

In order to represent an annular disk (or cylinder) using the hoop model, Karpp took the radius of gyration (r_g) as the radius of the hoop. Thus,

$$\sigma_o = \frac{\rho}{4} \frac{r_g^2}{r_c^2} \left(\frac{dD}{dt} \right)^2. \quad (9)$$

Similarly, substituting equations 1 and 6 into equations 4 and 5 yields

$$\sigma_o = \frac{\rho}{12k^2} \left(\frac{dD}{dt} \right)^2 \quad (10)$$

for the solid disk, and

$$\sigma_o = \frac{\rho}{16k^2} \left(\frac{dD}{dt} \right)^2 \quad (11)$$

for the solid cylinder under no net axial force. Thus, if the jet is solid, the strength estimate is only a function of the measured diametrical expansion rate and the number of fragments it produces.

3. Experiments

The molybdenum liners used in this test series were manufactured by Northwest Industries, Inc., Albany, OR. The starting material was 99.95% pure and had a grain size between 5 and 10 μm . From previous experience (Lampson, Harrison, and Krause 1992), the grain size in the finished liner is expected to be about the same, on average, as the starting material, although the grains in the liner are not equiaxed. The Vickers microhardness (100-g load) of a liner of this type was 203 kg/mm^2 (1,990 MPa), corresponding to an ultimate strength of about 645 MPa using the steel table (American Society for Metals 1983). Typical yield strengths for molybdenum vary from 500 to 700 MPa (Gulyaev 1980). The liner had a uniform wall thickness of 1.45 mm and an apex angle of 30° . It was truncated at the apex at an outside diameter of 20.2 mm and faired into a spherical cap and truncated at the base at an outside diameter of 90.4 mm.

The liner was installed in an aluminum body that was filled with 75/25 octol explosive (75% by weight HMX, $\text{C}_4\text{H}_8\text{N}_8\text{O}_8$, and 25% TNT, $\text{C}_7\text{H}_5\text{N}_3\text{O}_6$). An RP-80 detonator and a PBXN-5 booster were used to initiate the explosive. A typical shaped charge device is shown schematically in Figure 1. All of the shaped charges used in this series were nominally identical except for the detonator/booster holder, which was modified for spinning to allow the device to be coupled to a spin motor. The spin apparatus is described in Summers et al. (1994). Four devices were tested. Two devices were fired statically, and the other two were detonated while the shaped charge was spinning about its axis of symmetry. The shape and position of the jet produced by detonating the device was recorded by sequential flash radiography. Since simultaneous, orthogonal radiographs

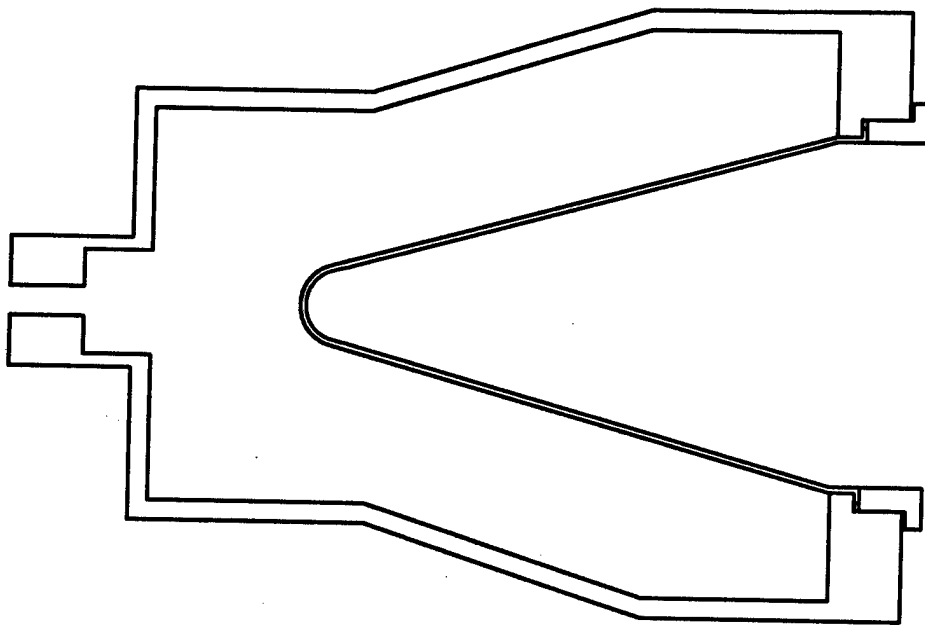


Figure 1. Schematic Diagram of a Shaped Charge Device.

were not available in these experiments, the Karpp-Simon method of estimating the spin rate was used.

4. Jet Measurements

Figure 2 shows that the front of the jet from a nonspinning device is composed of a pellet terminating in a boattail and followed by a region of initially high-velocity-gradient material, which rapidly thins as it stretches. This image was taken 180 μ s after the firing pulse was sent to the detonator. Figure 3 shows the pellet from another nonspinning device, observed at 936 μ s after initiation. This pellet buckled prior to the observation time, and its length at this time is roughly half its initial length. When the device was spun at 42 revolutions per second (rps) and detonated, the pellet remained intact, but the boattail region and the high-velocity gradient material burst into fragments under the influence of the centrifugal force (Figure 4). By 140 μ s after initiation, the pellet has begun to buckle (probably due to the air pressure) and the tip of the pellet is no longer on the axis of rotation. The pellet continued to deform, and the tip was pulled farther off axis, as shown

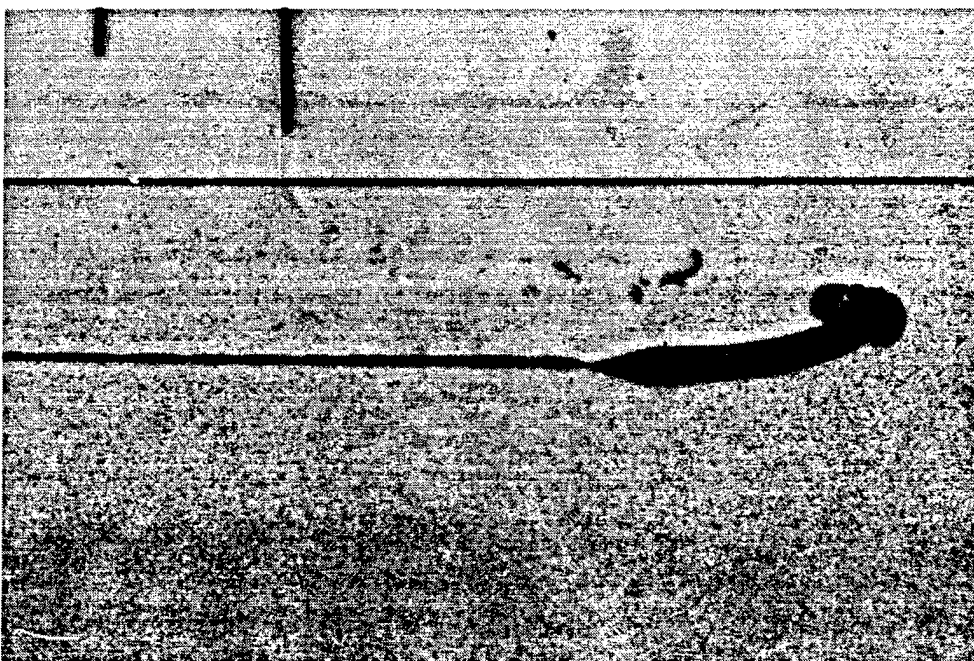


Figure 2. Flash Radiograph of Nonrotating Jet Pellet Taken at $t = 180 \mu\text{s}$.

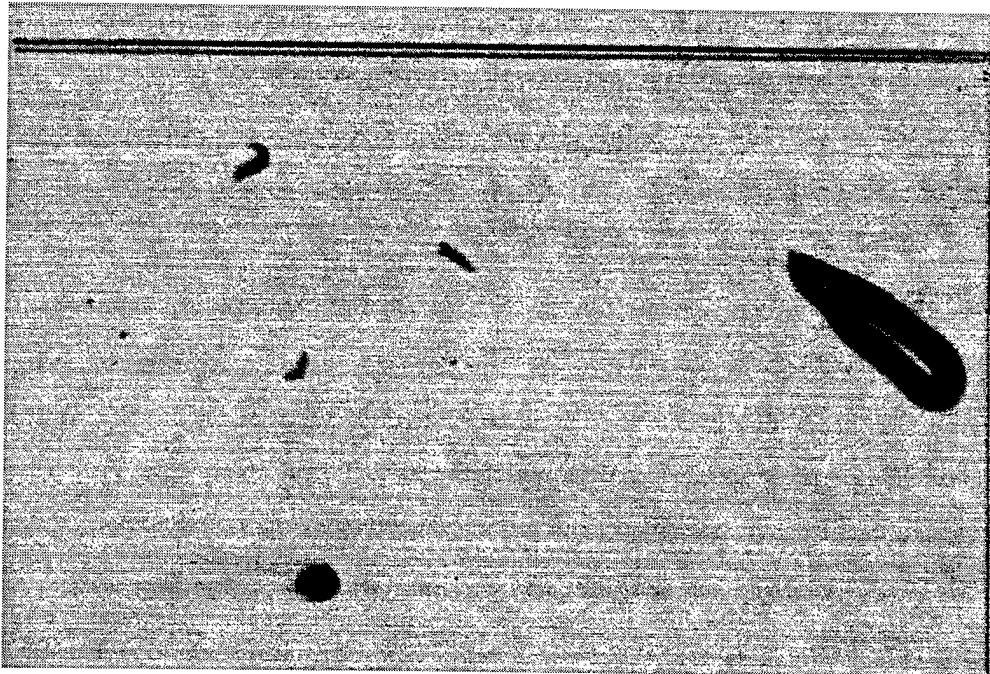


Figure 3. Flash Radiograph of Nonrotating Jet Pellet Taken at $t = 936 \mu\text{s}$.

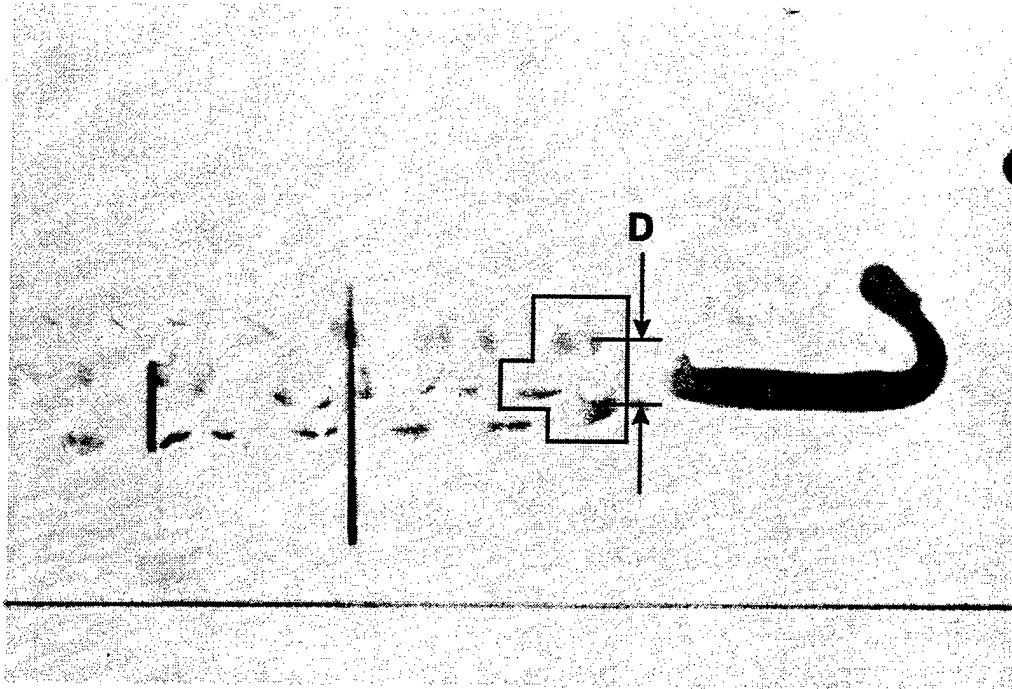


Figure 4. Flash Radiograph of Pellet From Device Spinning at 42 rps Taken at 140 μ s.

in Figure 5, due to the centrifugal force. When the device was spun at 60 rps, the pellet deformed to a radius over 60% larger than that at zero or 42 rps (Figure 6) and failed at the rear as evidenced by the large fragment widths. The pellet was not stable and continued to disintegrate and fail in "banana-peel" fashion at the rear and to increase in diameter still further at the front (Figure 7).

It was possible to identify and track individual fragments in the experiment in which the initial spin rate was 42 rps; this was not possible in the 60-rps experiment. Figures 4 and 5 show the debris fragments immediately behind the pellet. The three fragments indicated by the box in Figures 4 and 5 have, at 140 μ s, in the plane of the film, lengths of 8.2 mm, 10.0 mm, and 9.1 mm, with corresponding widths of 4.6 mm, 4.6 mm, and 1.8 mm. At 220 μ s, and viewed from another angle, the observed lengths are 9.1 mm, 8.2 mm, and 8.2 mm, with corresponding widths of 2.7 mm, 4.6 mm, and 2.7 mm (all with an uncertainty of ± 0.5 mm). The diametrical expansion rate in the vicinity of these three particles was measured to be 180 m/s.

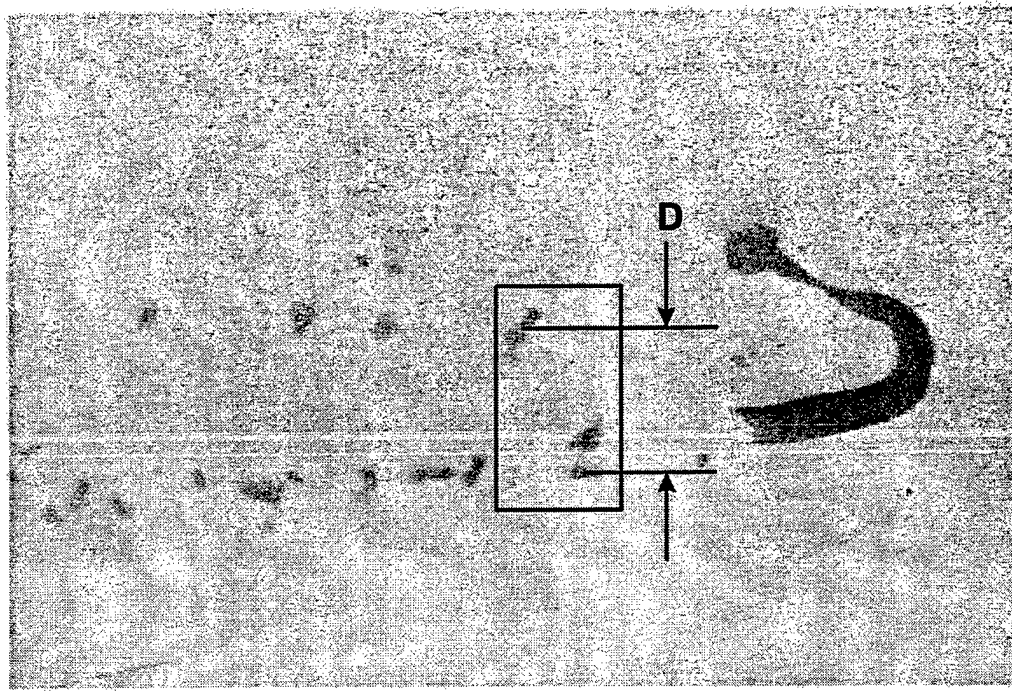


Figure 5. Flash Radiograph of Pellet From Device Spinning at 42 rps Taken at 220 μ s.

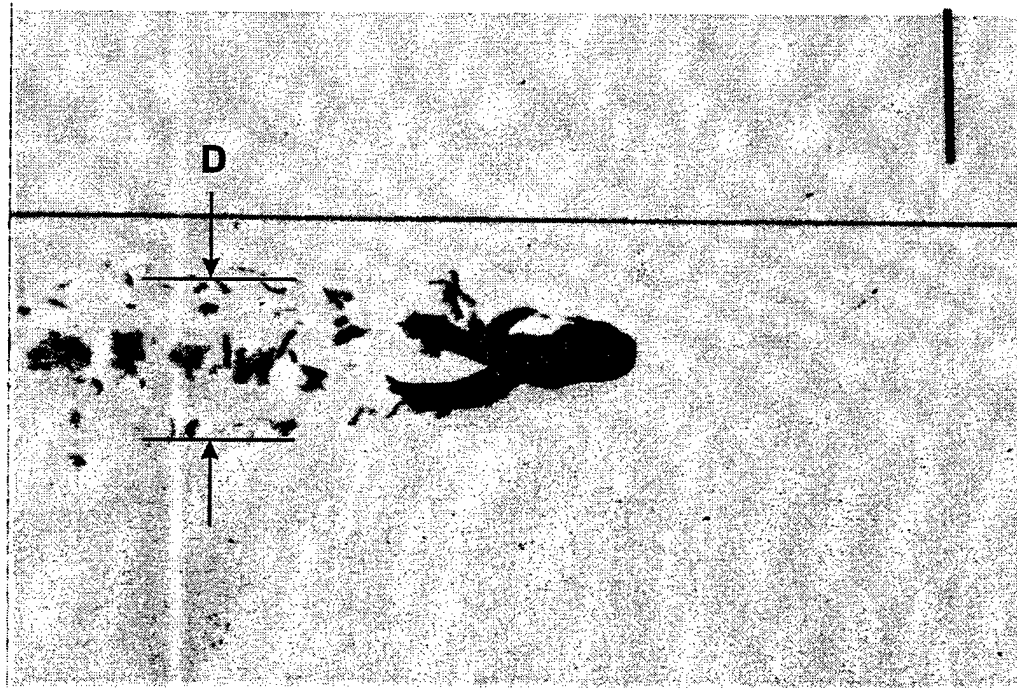


Figure 6. Flash Radiograph of Pellet From Device Spinning at 60 rps Taken at 160 μ s.

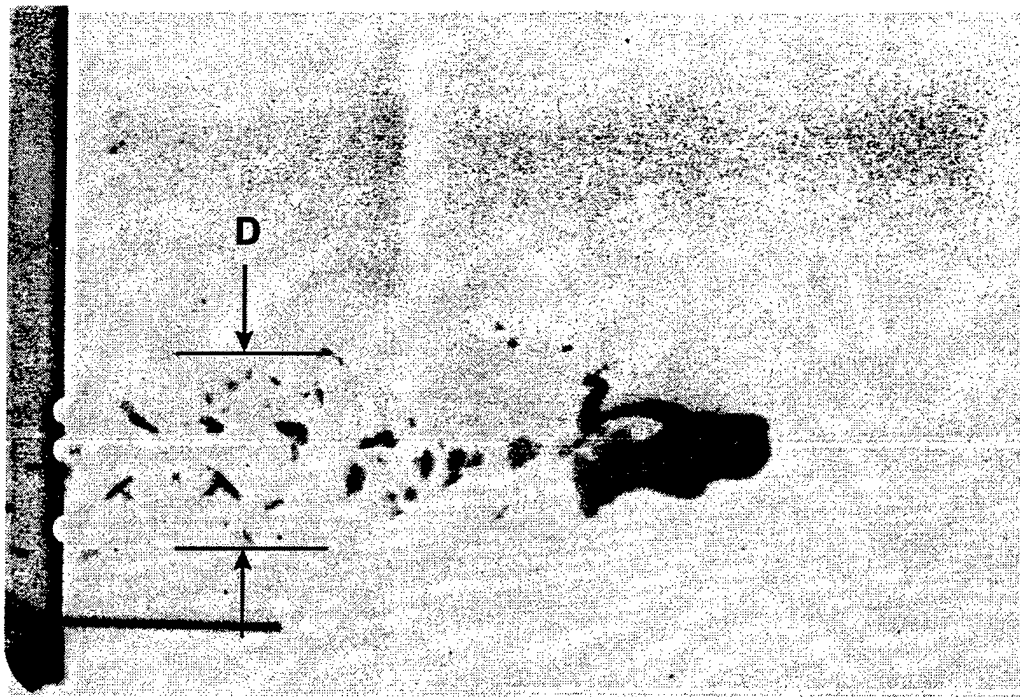


Figure 7. Flash Radiograph of Pellet From Device Spinning at 60 rps Taken at 200 μ s.

The measurements taken on the jet particles are summarized in Table 1. A cylindrical coordinate system was chosen with the z-axis aligned with the axis of symmetry of the liner. The quantities v_z and l refer to the axial velocity and length of the pellet plus boattail (when the boattail exists), while d is a representative diameter. The length of the pellet is measured at the first time of observation. The quantity $\frac{dD}{dt}$ is a measure of the diametrical expansion rate of the debris immediately behind the pellet. The estimated uncertainty in d is about 7%. The estimated uncertainty in $\frac{dD}{dt}$ is about 15% for shot 4691 and is somewhat larger for shot 4690.

5. Strength Estimates From Radiographic Measurements

In order to calculate the yield strength, an approximation to the critical angular velocity, ω_f , is obtained from the value of $\frac{dD}{dt}$ measured for the first jet segment that bursts (see Figure 4). A yield

Table 1. Experimental Data

Shot No.	ω (rps)	v_z (m/s)	ℓ (mm)	d (mm)	$\frac{dD}{dt}$ (m/s)
4690	60	10,000	47	12	230
4691	42	10,300	76	7.3	180
4692	0	—	59	7.0	—
4693	0	10,000	80	6.0	—

strength is then computed from the formula appropriate for the presumed geometry. Since the estimate of the critical angular velocity is determined from jet material that has burst, the yield strength computed from the experimental data is larger than the actual yield strength, which the element can support without bursting.

The jet fragments have a significant axial dimension, so the cylinder model is deemed the most appropriate. Using the data from the 42-rps experiment, if the jet segment is assumed to be a solid cylinder that fractures into two symmetrical pieces along a diameter, then the fragment width of 4.6 ± 0.5 mm corresponds to a outer radius of 2.3 ± 0.3 mm. Since the jet is assumed to be solid, the outer radius does not enter into the calculation for the stress. For two fragments, equation 7 gives $k = 0.4244$, and since $\frac{dD}{dt} = 180 \pm 27$ m/s using equation 1, the estimated angular velocity is $92,000 \pm 26,000$ rad/s. If there is no net axial force ($T = 0$) and the jet density is $10,200$ kg/m³, equation 11 gives a stress of 115 ± 35 MPa.

The jet fragments seem to form three columns (Figure 4), so another possibility is that the segment is a solid cylinder, which fractures into three symmetrical pieces. Then the maximum fragment width of 4.6 ± 0.5 mm corresponds to the length of a 120° chord and the outer radius is 2.7 ± 0.3 mm. The estimated angular velocity is $60,000$ rad/s $\pm 26\%$. The yield strength corresponding to this geometry is less than 68 ± 20 MPa.

The fact that the observed fragment widths include the value 1.8 mm suggests a hollow geometry. If it is assumed that the jet segment is hollow, that it burst symmetrically into three pieces, and that the minimum fragment width, 1.8 ± 0.5 mm, is the wall thickness of the jet, then, since the chord is 4.6 ± 0.5 mm, the outer radius lies between 3.0 mm and 2.4 mm, and the corresponding inner radii are 1.2 ± 0.5 mm and 0.6 ± 0.5 mm. Taking the extreme values (namely, $r_2 = 3.0$ mm with $r_1 = 1.7$ mm and $r_2 = 2.4$ mm with $r_1 = 0.1$ mm) the center-of-mass radius varies between 2.0 mm and 1.3 mm. The corresponding angular velocities are 45,000 rad/s and 69,000 rad/s, with uncertainties of 15%. The yield strengths corresponding to these geometries are less than 120 MPa and less than 76 MPa, with uncertainties of 30%. This variation in jet geometry combined with the measurement uncertainties provides a range of upper strength limits from about 50 MPa to 160 MPa.

It is observed in the radiographs that the front of the jet pellet deforms easily under the action of the aerodynamic forces. For hypersonic flight, the Newtonian approximation for the air pressure, $\rho_{\text{air}} v_z^2$, is appropriate (Vinh et al. 1980). At a sea-level flight speed of 10 km/s, this pressure is 120 MPa. This lies at about the midpoint of the strength range.

6. Strength Estimates From Calculations and Radiographic Data

If the radiographic data is combined with the results of a jet-formation calculation, the above range of possible geometries and yield strengths can be reduced. In addition, since the rear of the pellet did not fail at the lower spin rate (42 rps), but did at the upper spin rate, this information can be used to determine the strength if the geometry and the spin rate of the rear of the pellet can be estimated.

The calculation of the jet formation was made using a modified version of the BASC code (Harrison 1981), the changes being the inclusion of the acceleration of the liner (Kelley, Curtis, and Bremer 1994), the determination of the collapse conditions at an off-axis point and the effect of cylindrical symmetry in thickening the liner as it moves toward the axis of symmetry (Lampson

1987), and the incorporation of a centrifugal force resisting the collapse. The straight portion of the liner was divided into 100 independent ring elements, and the motion of the element boundaries was computed. For the subcalibered liner used in these devices, the effects of end rarefactions do not influence the characteristics of the jet in the region of interest and were accounted for by reducing the terminal velocities of the elements near the base of the liner by a factor that depended on the distance from the end of the charge.

The jet velocities predicted for the liner elements are displayed in Figure 8 at the corresponding z coordinates and are superimposed on an outline of the charge contour and the liner. The origin of the z-axis is at the beginning of the conical portion of the liner. The velocity increases until the shoulder of the body is reached; thereafter, it decreases because of the decreasing thickness of explosive covering the liner (the first discontinuous step) and then drops due to the combined effect of reduced explosive-layer thickness and rarefactions from the end of the charge. The shape of the velocity distribution explains the formation of the pellet because as the collapse proceeds from the apex to the shoulder of the body, faster-moving elements, formed at later times, overtake previously formed, slower elements. The relatively small decrease in velocity at the shoulder of the body formed a boattail at the rear of the pellet. The large drop formed the rapidly stretching part of the jet. The velocity of the pellet, determined by conservation of linear momentum of its constituents, was 10,400 m/s. The as-formed shape of the jet (i.e., the shape calculated at creation assuming no interaction between the elements) is shown above the velocity curve.

The devices were designed to be symmetric about the axis of rotation, so the detonation of the explosive is expected to produce no appreciable net external torque on the liner. No asymmetric internal stresses are expected in the liner due to the manufacturing process. Although accelerated during the collapse and jet-formation processes, the center of mass of each liner element always remains on the axis of symmetry; therefore, the angular momentum of each independent liner element is conserved. The jet segments are assumed to spin independently of each other because the material strength is expected to be sufficiently low that coupling between the spins of neighboring elements can be neglected in the time scale of interest, less than 100 μ s.

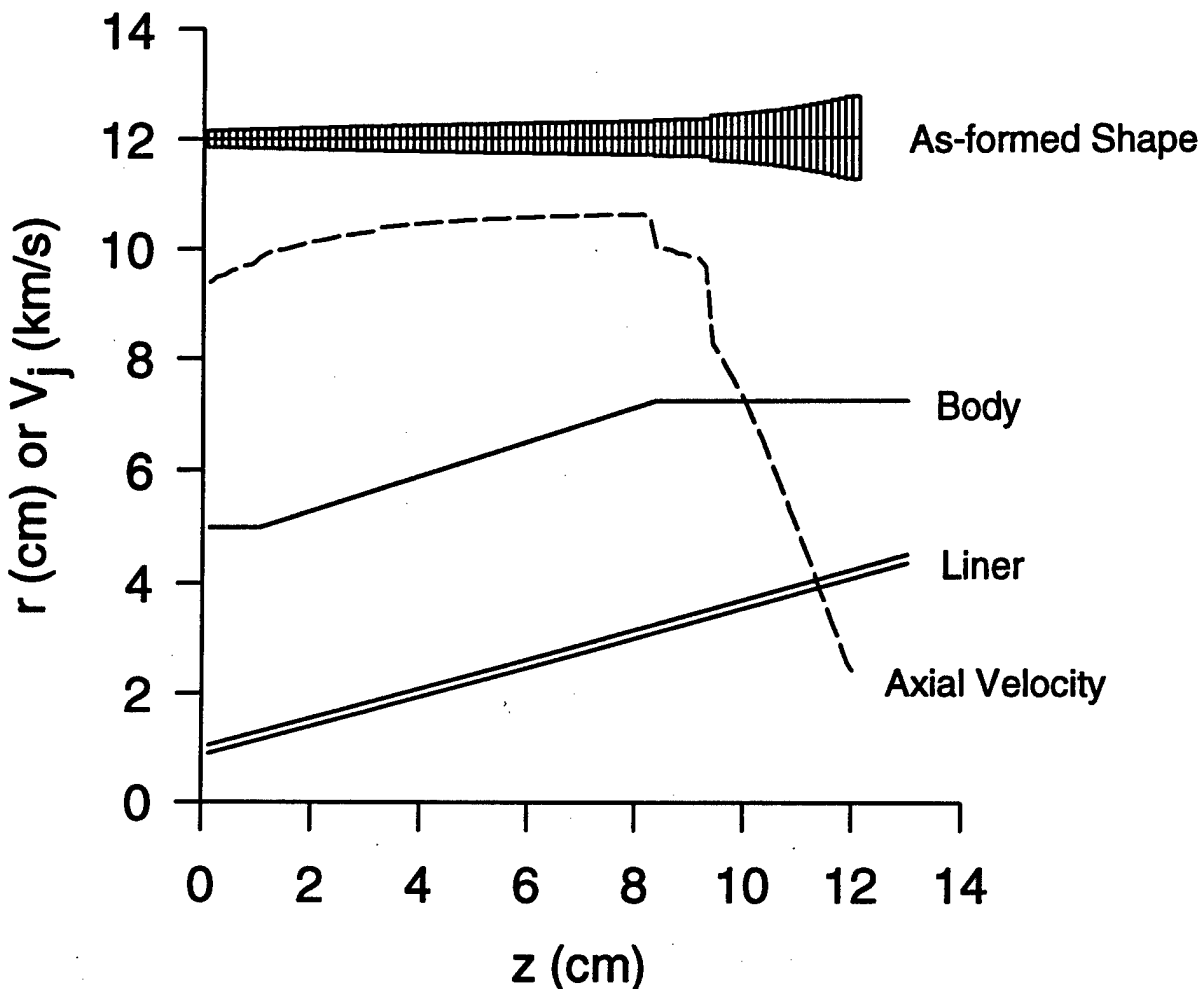


Figure 8. Calculated Jet Velocity as a Function of Position Along the Liner and Computed Pellet Shape.

The calculations show that the collapse process was not perturbed appreciably at the spin rates used in these experiments. The spin rate of each jet element was computed by calculating its moment of inertia (I) in its initial position when the inner and outer radii were R_1 and R_2 (Figure 9) and in its "collapse" position when the inner and outer radii were R_{C1} and R_{C2} . In the collapse configuration, the portion of the liner that entered the jet was separated as a ring element with inner and outer radii R_{C1} and R_{C3} . The jet was assumed to form on the axis of symmetry as a solid cylinder with outer radius r_j .

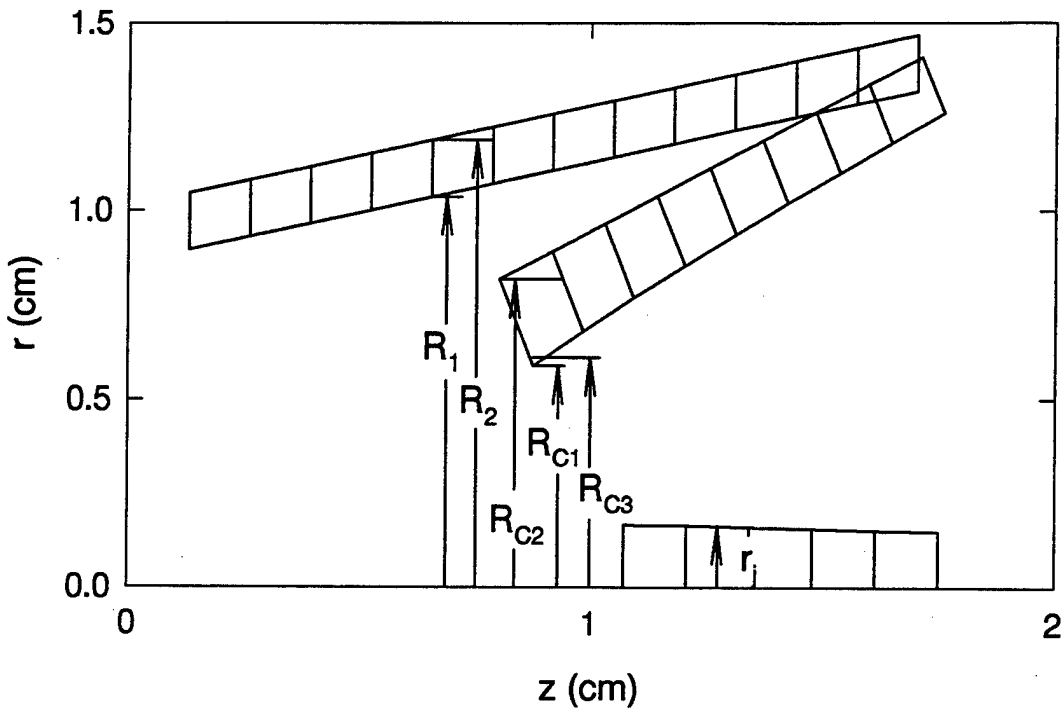


Figure 9. Collapse Sequence Computed for Liner Element 5 and Resulting Jet Element.

Given the moment of inertia at each stage of the jet-formation process, the corresponding spin rate was computed for each jet element by conserving the angular momentum. Detailed results are given in Appendix C. The as-formed spin rates for solid jet elements are shown in Figure 10. For both of the initial liner spin rates, the spin rate of the jet elements first increases with axial position because the corresponding initial radial coordinates of the liner elements increase, and the fraction of the liner material entering the jet is roughly constant. The spin rate peaks at the tail of the pellet and drops thereafter because the fraction of liner material entering the jet increases, creating a larger disk with a larger moment of inertia. The spin rate rises again because the fraction of liner material stabilizes at a constant value on the velocity step shown in Figure 8. Thereafter, the jet-mass fraction increases rapidly with a consequent lowering of the spin rate.

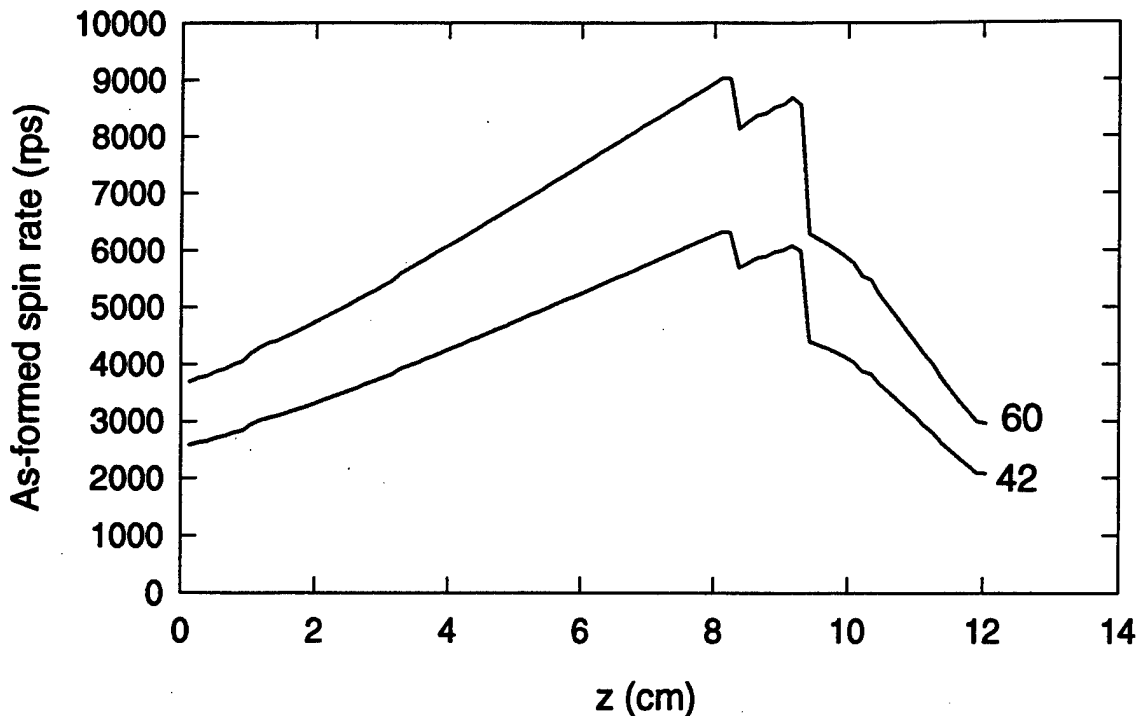


Figure 10. Calculated As-Formed Spin Rate of Jet as a Function of Position Along the Liner and Initial Liner Spin Rate.

The jet pellet is composed of liner elements 1–63. Liner elements 64–71 are associated with the boattail since their velocities correspond to the measured axial velocities of the boattail fragments. The liner elements at the tail of the pellet and in the boattail have the highest as-formed spin rates. The computed values of outer and inner radii and spin rate for liner elements 61–71 at various stages in the jet-formation process are listed in Table 2.

According to the calculation, the boattail is composed of up to eight elements. The length of each segment of the liner was 1.31 mm and the maximum observed fragment length immediately behind the pellet was 10 mm, so if the jet did not stretch before bursting, a fragment of length 10 mm comprises about six segments. The average axial velocity of the six-element boattail is 9.94 km/s, while the axial velocity of the center of mass of the three fragments is 10.1 ± 0.2 km/s, so this correspondence seems reasonable. The average as-formed radius of the six-element boattail is 3.3 mm, lower than the observed radius at the rear of the pellet in this experiment, 3.65 mm, so, according to the calculation, the boattail should be hollow.

Table 2. Computed Radii and Angular Velocities of Elements 61–71

N	R ₂ (cm)	R ₁ (cm)	ω _o (rps)	R _{C2} (cm)	R _{C1} (cm)	ω ₁ (rps)	r _j (cm)	ω ₂ (rps)	r _{obs} (cm)	V _z (km/s)
61	3.15	3.00	42	1.36	0.99	281	0.30	6,260	0.365	10.622
62	3.19	3.04	42	1.37	0.99	285	0.31	6,320	0.365	10.626
63	3.22	3.07	42	1.37	1.00	288	0.31	6,320	0.365	10.569
64	3.26	3.11	42	1.38	1.01	291	0.33	5,700	—	10.012
65	3.29	3.14	42	1.39	1.01	294	0.33	5,780	—	9.996
66	3.33	3.18	42	1.40	1.02	298	0.33	5,860	—	9.981
67	3.36	3.21	42	1.40	1.02	301	0.33	5,890	—	9.917
68	3.40	3.25	42	1.41	1.03	304	0.34	5,970	—	9.900
69	3.43	3.28	42	1.42	1.03	307	0.34	6,000	—	9.843
70	3.47	3.32	42	1.43	1.04	311	0.34	6,080	—	9.825
71	3.50	3.35	42	1.43	1.04	314	0.35	5,990	—	9.673

The diameter of the cylinder containing the estimated centers of mass of the three fragments is roughly 13 ± 1 mm at 140 μ s, and about 27 ± 1 mm at 220 μ s. If the average tangential velocity of the fragments is 90 m/s (0.090 ± 0.015 mm/ μ s), and the initial location of the centers of mass was at a radius of gyration of 2.35 mm (corresponding to an initial solid radius of 3.32 mm), then the transit time to a radius of 6.5 ± 0.5 mm is 47 ± 14 μ s and 124 ± 26 μ s to 13.5 ± 0.5 mm. Subtracting these transit times from the times of observation (flash times), a burst time for the jet element of about 95 μ s after the device was initiated is representative. From its position at these flash times, the boattail was formed at about 35 μ s, so the jet elements stretched for about 60 μ s before bursting.

For an extending jet of uniform radius with a linear velocity gradient in the axial direction, the length L at time t after formation is (Curtis 1987)

$$L = L_o (1 + \eta t), \quad (12)$$

where

$$\eta = \Delta v / L_o,$$

Δv being the velocity difference between the ends of the jet and L_0 , the initial length. If a six-element boattail (elements 64–69) stretched for 60 μs , its length would be about 2.3 times its initial length of 7.86 mm, or 18 mm. This exceeds the maximum observed fragment length, so the fragments must represent a smaller fraction of the boattail.

If the first four elements of the boattail, elements 64–67, are used to represent the fragments, the average axial velocity is 9.98 km/s and the length at burst is about 2.0 times the initial length, or about 10.5 mm. This length is consistent with the maximum fragment length, 10.0 ± 0.5 mm, and the average velocity is consistent with the measured average axial velocity of the center of mass of the fragments, 10.1 ± 0.2 km/s.

From Table C-1, the average as-formed radius of jet elements 64–67 is 3.32 mm and the average as-formed spin rate is 5,810 rps (36,500 rad/s), when the liner is initially spinning at 42 rps. Assuming incompressible extension of the solid, as-formed jet to twice its initial length, the radius at burst is 2.35 mm. Since the moment of inertia of a solid cylinder is proportional to the square of the radius, the spin rate at burst is 72,900 rad/s, from conservation of angular momentum. If the boattail is assumed to be composed of these solid elements and it fails with an outer radius of 2.35 mm (consistent with the minimum experimentally inferred radius), then the spin rate at failure is 72,900 rad/s and the yield strength (from equation 5 with $T = 0$) is less than 75 MPa. Assuming that this solid boattail breaks into 120° segments, $r_c = 1.29$ mm (equation 6) and the “fly-off” velocity, $r_c \omega_f$, is 94 m/s.

The boattail is formed with a mass that corresponds to an average radius of 2.35 mm and a spin rate of 72,900 rad/s at failure, if it is solid. If the boattail is assumed to be hollow when it fails, with an outer radius of 2.70 mm (see the discussion in section 5), then conservation of mass requires that its inner radius be 1.33 mm. The resulting wall thickness of 1.4 mm is within the range of the wall thickness inferred from the radiographic measurements, 1.8 ± 0.5 mm.

The moment of inertia for a hollow cylinder is proportional to the sum of the squares of the inner and outer radii. Conservation of angular momentum gives the spin rate at failure, 44,400 rad/s.

Using the tangential velocity of the center of mass of a 120° segment, equations 8 and 5, the fly-off velocity is 77 m/s, consistent with the measured value of 90 ± 14 m/s. Numerical solution of the equations for the stress in an annular cylinder (see Appendix B) shows that the yield stress is less than 86 MPa.

An annular cylinder with an outer radius larger than 2.7 mm produces 120° fragments with a fly-off velocity below the lower limit of the measurements. Thus, the calculation selects a fairly narrow range of jet geometries consistent with the observed fly-off velocity.

At an initial device spin rate of 42 rps, the rear of the pellet remained intact over the period of observation, while when the initial spin rate was 60 rps, it failed. With this in mind, we can reduce the range of the strength value by considering the behavior of the rear of the pellet. According to the calculation, the as-formed solid radius of the rear of the pellet is 3.09 mm (element 63 in Table C-1). The observed diameter given in Table 1 for shot 4691 is 7.3 mm $\pm 7\%$. The observed radius lay in the range 3.39 mm to 3.91 mm. Conservation of mass and incompressibility indicate that the rear of the pellet is hollow with corresponding inner radii of 1.39 mm and 2.40 mm. The calculated as-formed radius of gyration (equation C-16) and spin rate (element 63 in Table C-1) were 2.18 mm and 39,700 rad/s for a solid jet segment when the initial liner spin rate was 42 rps. If the segment is hollow with a radius of gyration of 2.59 mm (corresponding to an outer radius of 3.39 mm), the spin rate is 28,100 rad/s, while if the radius of gyration is 3.24 mm, the spin rate is 18,000 rad/s. The strength lies in the range of 33–48 MPa. Therefore, the strength must be greater than about 30 MPa.

When the initial liner spin rate was 60 rps, the as-formed angular velocity of the rear of the pellet was 56,700 rad/s (Table C-1). Assuming the same geometries at failure as in the 42 rps case (i.e., an outer radius of 3.39 mm), for the smaller radius of gyration, the spin rate is 40,200 rad/s, while for the larger radius of gyration, it is 25,700 rad/s. This puts the material strength at less than 68 MPa, or less than 98 MPa, depending on the geometry. The strength must be less than about 100 MPa. Thus, the strength limits obtained from a combination of the jet-formation calculations and the radiographic data are

$$30 \text{ MPa} < \sigma_o < 100 \text{ MPa.}$$

7. Discussion

The reliability of the yield strength estimated from the formulas depends on the accuracy of the geometry assumed for the jet and the measurement of the jet spin rate. The cylinder model seems to be the most appropriate model for assessing the strength because the fragments and the pellet have appreciable length and radial extent. The existence of hollowness is important because the strength required to support a solid jet against spin forces is less than that required to support an annular jet. Both solid and annular geometries were considered. The hollow geometry seems more consistent with the observed fragment widths than the solid.

In Section 5, the jet spin rate is inferred from the diametrical expansion rate. Using the diametrical expansion rate for this purpose when there are only three fragments results in a systematic error tending to underestimate the angular velocity. The magnitude of this error is difficult to quantify but would tend to increase the jet strength, since the spin rates would increase somewhat.

Only the boattail burst when the initial liner spin rate was 42 rps. Using the radiographic data alone to calculate the yield strength gives a range of values from zero to less than 160 MPa. This range of values is compatible with the observed deformation of the pellet under the action of aerodynamic forces of magnitude, roughly 120 MPa.

The first case considered in section 5 was a solid cylindrical segment with a radius of 2.3 ± 0.3 mm and a spin rate of $92,000 \pm 26,000$ rad/s. Equation 11 then gave a strength of less than 115 ± 35 MPa. The calculation gives, for a solid jet segment in the boattail, a radius at burst of 2.35 mm and a spin rate of 72,900 rad/s. Using the calculated values in equation 11 gives a stress of about 75 MPa at the low end of radiographic strength range.

The second case examined in section 5 was a solid cylindrical segment with a radius of 2.7 ± 0.3 mm and a spin rate of $60,000 \pm 16,000$ rad/s. The estimated yield strength was less than 68 ± 20 MPa. The stress based on the jet-formation calculation fits comfortably within this range.

The third case considered in section 5 was an annular cylindrical segment. The extreme values of outer/inner radii were 3.0 mm/1.7 mm and 2.4 mm/0.1 mm and the corresponding average spin rates were 45,000 rad/s and 69,000 rad/s. The yield strengths were less than 120 MPa and less than 76 MPa, respectively.

Using the radiographic measurements and the jet-formation calculations, the range of the yield strength can be reduced, as shown in section 6. The calculation indicated a hollow boattail segment with an outer radius no larger than 2.70 mm, in order to be consistent with the observed fly-off velocity. The corresponding inner radius was 1.33 mm and the spin rate at burst was 44,400 rad/s. The calculation gives a yield stress of less than 86 MPa.

A solid boattail was also considered in section 6. In this case, the yield strength was less than 75 MPa and the fly-off velocity was 94 m/s. However, such a geometry is not consistent with the observed widths of the fragments.

Finally, the rear of the pellet was examined. The rear of the pellet remained intact when the initial liner spin rate was 42 rps. The minimum strength required to keep the pellet intact, using the calculated geometry and spin rate, is 30 MPa. The rear of the pellet yielded at 60 rps. According to the calculations, the strength must be less than 100 MPa.

The range of stresses from 30 to 100 MPa encompasses nearly all of the values obtained from the radiographic measurements. A yield strength much above 100 MPa seems unlikely from the calculations and from the observed aerodynamic behavior.

8. Conclusion

The combination of calculated and observed burst conditions indicates that the yield strength of the jet must be greater than 30 MPa and less than 100 MPa. Taking the midpoint value as representative, the yield strength of this molybdenum jet, evaluated near the tail of the pellet, appears to be about 65 MPa, with a probable uncertainty of about 60%.

9. References

- American Society for Metals. *ASM Metals Reference Book*. Second edition, Metals Park, OH, 1983.
- Curtis, J. P. "Axisymmetric Instability Model for Shaped Charge Jets." *Journal of Applied Physics*, vol. 61, no. 11, pp. 4978–4985, June 1987.
- Davis, E. A., and F. M. Connelly. "Stress Distribution and Plastic Deformation in Rotating Cylinders of Strain-Hardening Material." *Trans. ASME, Journal of Applied Mechanics*, vol. 26, Series E, no. 1, pp. 25–30, March 1959.
- Eichelberger, R. J. "Experimental Test of the Theory of Penetration by Metallic Jets." *Journal of Applied Physics*, vol. 27, no. 1, pp. 63–68, January 1956.
- Gulyaev, A. *Physical Metallurgy*. Vol. 2, Moscow: Mir Publishers, 1980.
- Harrison, J. T. "Improved Analytical Shaped Charge Code: BASC." BRL-TR-02300, U.S. Army Ballistic Research Laboratory, Aberdeen Proving Ground, MD, March 1981.
- Karpp, R. R., and J. Simon. "An Estimate of the Strength of a Copper Shaped Charge Jet and the Effect of Strength on the Breakup of a Stretching Jet." BRL-TR-1893, U.S. Army Ballistic Research Laboratory, Aberdeen Proving Ground, MD, June 1976.
- Kelley, R. J., J. P. Curtis, and M. Bremer. "On Analytic Modeling of Casing and Liner Thickness Variations in a Shaped Charge." *Journal of Applied Physics*, vol. 75, no. 1, January 1994.
- Lampson, M. L. "Jet Formation From Collapsing Conical Shells." *Proceedings of the 10th International Symposium on Ballistics*, vol. 3, San Diego, CA, 27–29 October 1987.
- Lampson, M. L., J. T. Harrison, and C. D. Krause. "Molybdenum Shaped-Charge Jets." BRL-TR-3403, U.S. Army Ballistic Research Laboratory, Aberdeen Proving Ground, MD, September 1992.
- Nadai, A. *Theory of Flow and Fracture of Solids*. Vol. 1, New York: McGraw-Hill Book Co, Inc., 1950.
- Summers, R. L., W. P. Walters, L. W. Burke, Jr., C. V. Paxton, and J. W. Gardiner. "Static Detonation of Spinning Warheads." ARL-TR-372, U.S. Army Research Laboratory, Aberdeen Proving Ground, March 1994.
- Walsh, J. M. "Plastic Instability and Particulation in Stretching Metal Jets." *Journal of Applied Physics*, vol. 56, no. 7, pp. 1997–2006, 1 October 1984.

Vinh, X. Nguyen, A. Buseman, and R. D. Culp. *Hypersonic and Planetary Entry Flight Mechanics*. Ann Arbor: The University of Michigan Press, 1980.

Appendix A:

Stresses in Solid and Annular Disks

INTENTIONALLY LEFT BLANK.

In this appendix, the equations relating the yield strength of a material to the angular velocity that causes a thin disk rotating about its axis to become partially or totally plastic are derived. The elastic and elastic perfectly plastic stress distributions in the disk are examined to the point where the disk becomes fully plastic. Elastic solutions of the stress distributions in both solid and annular disks are well known and may be found in several texts (Nadai,¹ Johnson and Mellor,² and den Hartog³). In addition, the elastic-plastic solution for the solid disk is also given by both Nadai¹ and Johnson and Mellor.² The annular rotating disk was also treated by both Nadai¹ and Johnson and Mellor,² however, both texts contained errors in their final expressions for the position of the elastic-plastic boundary.

1. Elastic Stress Distribution in Rotating Disks

The stress distribution in the rotating shaped charge jet may be calculated if a segment of the rotating jet at the time of burst is represented as a rotating disk. Only two components of stress need to be considered: (1) the tangential stress (σ_t) and (2) the radial stress (σ_r). The equilibrium equation in this case is

$$\frac{d}{dr}(r\sigma_r) - \sigma_t + \rho\omega^2r^2 = 0, \quad (A-1)$$

where ρ is the mass density, ω is the angular velocity, and r is the radial coordinate. If the radial displacement is sufficiently small, then the radial displacement (u) is related to the radial and tangential strains by

$$\epsilon_r = \frac{du}{dr}, \quad (A-2)$$

¹ Nadai, A. *Theory of Flow and Fracture of Solids*. Vol. 1, New York: McGraw-Hill Book Company, Inc., 1950.

² Johnson, W., and P. B. Mellor. *Engineering Plasticity*. New York: Van Nostrand Reinhold Company, 1973.

³ Den Hartog, J. P. *Advanced Strength of Materials*. New York: Dover Publications, Inc., 1952.

and

$$\varepsilon_t = \frac{u}{r}, \quad (A-3)$$

respectively. Hooke's law then gives

$$\frac{du}{dr} = \frac{\sigma_r - v\sigma_t}{E}, \quad (A-4)$$

and

$$\frac{u}{r} = \frac{\sigma_t - v\sigma_r}{E}, \quad (A-5)$$

where E is Young's modulus and v is Poisson's ratio. Equations A-1, A-4, and A-5 are solved for σ_r , since the boundary conditions involve σ_r . Differentiating equation A-5 gives

$$\frac{1}{r} \frac{du}{dr} - \frac{u}{r^2} = \frac{1}{E} \left(\frac{d\sigma_t}{dr} - v \frac{d\sigma_r}{dr} \right). \quad (A-6)$$

Substituting for $\frac{du}{dr}$ from equation A-4, one obtains

$$\frac{1}{r} \left(\frac{\sigma_r - v\sigma_t}{E} \right) - \frac{u}{r^2} = \frac{1}{E} \left(\frac{d\sigma_t}{dr} - v \frac{d\sigma_r}{dr} \right). \quad (A-7)$$

Substituting for $\frac{u}{r}$ from equation A-5 and rearranging yields

$$\frac{d\sigma_t}{dr} - v \frac{d\sigma_r}{dr} + \frac{(1+v)}{r} (\sigma_t - \sigma_r) = 0. \quad (A-8)$$

Solving equation A-1 for σ_t and differentiating the result with respect to r gives

$$\frac{d\sigma_t}{dr} = \frac{d^2}{dr^2}(r\sigma_r) + 2\rho\omega^2r. \quad (\text{A-9})$$

Substitution of this into equation A-8 eliminates $d\sigma_t/dr$ from the equation, and using equation A-1 to define σ_r , one obtains

$$\frac{d^2}{dr^2}(r\sigma_r) + 2\rho\omega^2r - v\frac{d\sigma_r}{dr} + \frac{(1+v)}{r}\left(\frac{d}{dr}(r\sigma_r) + \rho\omega^2r^2 - \sigma_r\right) = 0. \quad (\text{A-10})$$

Noting that

$$\frac{d}{dr}(r\sigma_r) = \sigma_r + r\frac{d\sigma_r}{dr} \quad (\text{A-11})$$

gives

$$\frac{d\sigma_r}{dr} = \frac{1}{r}\left(\frac{d}{dr}(r\sigma_r) - \sigma_r\right). \quad (\text{A-12})$$

Substituting this into equation A-10 and multiplying by r^2 gives

$$r^2\frac{d^2}{dr^2}(r\sigma_r) + r\frac{d}{dr}(r\sigma_r) - r\sigma_r + (3+v)\rho\omega^2r^3 = 0. \quad (\text{A-13})$$

It can be readily verified that the solution of equation A-13 is then

$$r\sigma_r = C_1r + \frac{C_2}{r} - \frac{(3+v)\rho\omega^2r^3}{8}, \quad (\text{A-14})$$

with the two integration constants determined by the boundary conditions. Solving equation A-1 for σ_t gives

$$\sigma_t = \frac{d}{dr}(r\sigma_r) + \rho\omega^2r^2, \quad (A-15)$$

so

$$\sigma_t = C_1 - \frac{C_2}{r^2} - \frac{(1 + 3v)\rho\omega^2r^2}{8}, \quad (A-16)$$

while

$$\sigma_r = C_1 + \frac{C_2}{r^2} - \frac{(3 + v)\rho\omega^2r^2}{8}. \quad (A-17)$$

From equation A-5,

$$u = \frac{r}{E} \left((1 - v)C_1 - (1 + v)\frac{C_2}{r^2} - \frac{(1 - v^2)\rho\omega^2r^2}{8} \right). \quad (A-18)$$

1.1 Elastic Stress Distribution in Solid Disks

The boundary conditions for a solid disk are that the stresses remain finite at $r = 0$ and that $\sigma_r = 0$ at $r = r_o$, the outside radius. The solution becomes³

$$\sigma_r = \frac{(3 + v)\rho\omega^2(r_o^2 - r^2)}{8}, \quad (A-19)$$

³ Den Hartog, J. P. *Advanced Strength of Materials*. New York: Dover Publications, Inc., 1952.

$$\sigma_t = \frac{(3 + v)\rho\omega^2}{8} (r_o^2 - \frac{1 + 3v}{3 + v} r^2), \quad (A-20)$$

and

$$u = \frac{(1 - v)r\rho\omega^2}{8E} ((3 + v)r_o^2 - (1 + v)r^2). \quad (A-21)$$

At the center of the disk, the stresses are the largest, and $\sigma_r = \sigma_t$ at that point. There is a state of two-dimensional hydrostatic tension with the stress

$$\sigma_{center} = \frac{(3 + v)\rho(r_o\omega)^2}{8}, \quad (A-22)$$

where $r_o\omega$ is the peripheral speed of the disk.

1.2 Elastic Stress Distribution in Annular Disks

The boundary conditions for an annular disk are that $\sigma_r = 0$ at $r = r_i$, the inside radius, and $\sigma_r = 0$ at $r = r_o$. In this case,

$$\sigma_r = \frac{(3 + v)\rho\omega^2}{8} \left(r_o^2 + r_i^2 - \frac{r_o^2 r_i^2}{r^2} - r^2 \right), \quad (A-23)$$

$$\sigma_t = \frac{(3 + v)\rho\omega^2}{8} \left(r_o^2 + r_i^2 + \frac{r_o^2 r_i^2}{r^2} - \frac{(1 + 3v)}{(3 + v)} r^2 \right), \quad (A-24)$$

and

$$u = \frac{(3 + v)(1 - v)\rho\omega^2 r}{8E} \left(r_o^2 + r_i^2 + \frac{1 + v}{1 - v} \left(\frac{r_o^2 r_i^2}{r^2} \right) - \frac{(1 + v)}{(3 + v)} r^2 \right). \quad (A-25)$$

These equations are also well known.³

2. Stress Distribution in Elastic Perfectly Plastic Disks

2.1 Solid Disks

Plastic flow is assumed to occur when the Tresca yield criterion is satisfied for this case of plane stress. According to Tresca, the material yields if the maximum shear stress, τ_{\max} , exceeds one-half the yield strength, σ_0 . The maximum shear stress is equal to one-half the difference between the largest and smallest of the principal stresses. The axial stress is zero by definition. The maximum values of the radial and tangential stresses occur at the center of the solid disk, so, at this point, the maximum shear stress is equal to half the stress at the center. Therefore, the solid disk first yields at the center when $\sigma_{center} = \sigma_0$, and, from equation A-22, the square of the peripheral speed is

$$(r_o \omega_c)^2 = 8 \sigma_0 / ((3 + v) \rho). \quad (A-26)$$

Defining the ratio of σ_0 to ρ as the square of a reference velocity (v_o) and defining the above peripheral speed as a critical velocity for the onset of plastic yielding (v_c), the relation between these two speeds is

$$v_c = v_o (8 / (3 + v))^{1/2}. \quad (A-27)$$

If $v = 1/3$, then $v_c = 1.55 v_o$.¹ The stresses, scaled by the factor $8/(\rho (3 + v) r_o^2 \omega_c^2)$, and the radial displacement, scaled by the factor $8E/(\rho (1 - v) (3 + v) r_o^3 \omega_c^2)$, are shown in Figure A-1, where ω_c is the angular velocity corresponding to the critical peripheral speed v_c .

¹ Nadai, A. *Theory of Flow and Fracture of Solids*. Vol. 1, New York: McGraw-Hill Book Company, Inc., 1950.

³ Den Hartog, J. P. *Advanced Strength of Materials*. New York: Dover Publications, Inc., 1952.

In most texts, the yield strength is known and the angular velocity at which the disk yields is unknown. However, in this report, it is assumed that the angular velocity that causes the disk to rupture can be measured and the yield strength is calculated. If the point of initial yielding is taken to be indicative of the rupture of the disk, then the yield strength for a solid disk is given by:

$$\sigma_o = \frac{(3 + v)\rho(r_o\omega_c)^2}{8}. \quad (A-28)$$

The actual rupture of the disk will occur at some point after the *entire* disk has yielded. As the angular velocity is increased, the boundary between the plastic inner region and the elastic outer region will move toward the outer radius of the disk. As shown in Figure A-1, the tangential stress is never smaller than the radial stress. Thus, the difference between the tangential and the axial stress reaches the yield strength before the difference between the radial and the axial stress does, and the yield criterion is always

$$\sigma_t = \sigma_o. \quad (A-29)$$

In the plastic region, the equilibrium equation takes the form

$$\frac{d}{dr}(r\sigma_r) - \sigma_o + \rho\omega^2r^2 = 0. \quad (A-30)$$

The solution for the radial plastic stress is then

$$\sigma_r = \frac{C}{r} + \sigma_o - \frac{\rho\omega^2r^2}{3}. \quad (A-31)$$

The radial stress must remain finite at $r = 0$ in the solid disk, so $C = 0$ and

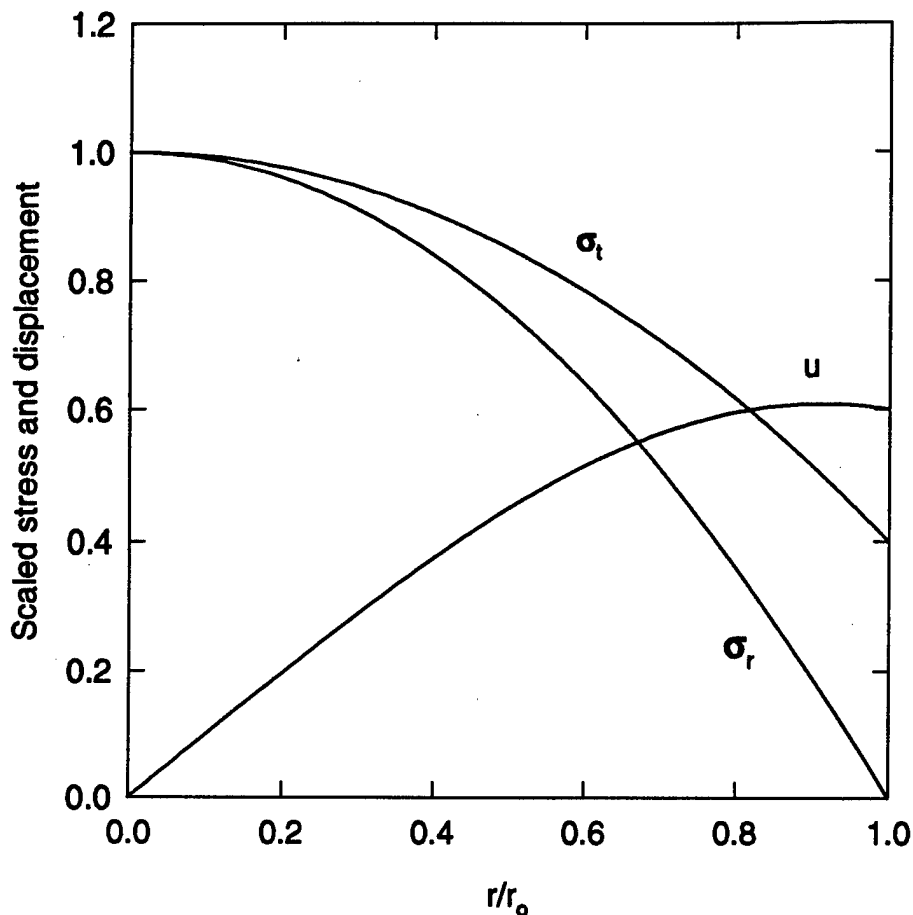


Figure A-1. Scaled Stresses and Displacements of the Spinning Solid Disk at the Critical Velocity.

$$\sigma_r = \sigma_o - \frac{\rho \omega^2 r^2}{3}. \quad (A-32)$$

In the elastic region, extending from the plastic boundary, $r = r_p$ to $r = r_o$, the stresses are given by equations A-16 and A-17, subject to new boundary conditions. Applying the condition that $\sigma_r = 0$ at $r = r_o$ gives, from equation A-17,

$$C_1 = \frac{(3 + v)}{8} \rho \omega^2 r_o^2 - \frac{C_2}{r_o^2}. \quad (A-33)$$

Applying the condition that $\sigma_t = \sigma_o - \frac{\rho\omega^2 r^2}{3}$ at $r = r_p$ gives, from equations A-17 and A-33,

$$C_2 = \frac{r_o^2 r_p^2}{r_o^2 - r_p^2} \left(\sigma_o - \rho\omega^2 \left(\frac{(3+v)}{8} (r_o^2 - r_p^2) + \frac{r_p^2}{3} \right) \right). \quad (\text{A-34})$$

Applying the condition that $\sigma_t = \sigma_o$ at $r = r_p$ gives, from equation A-16,

$$\rho\omega^2 = \frac{24\sigma_o r_o^2}{(3(3+v)r_o^4 - 2(1+3v)r_o^2 r_p^2 + (1+3v)r_p^4)}. \quad (\text{A-35})$$

In terms of the peripheral speed ($v^2 = \omega^2 r_o^2$) and the reference velocity (v_o^2),

$$v^2 = \frac{24v_o^2 r_o^4}{(3(3+v)r_o^4 - 2(1+3v)r_o^2 r_p^2 + (1+3v)r_p^4)}. \quad (\text{A-36})$$

The entire disk yields when $r_p = r_o$, the terms in v drop out in equation A-36, and the peripheral speed equals,

$$v = 1.73 v_o \quad (\text{A-37})$$

or

$$v = 1.12 v_c. \quad (\text{A-38})$$

This result was also obtained by Nadai.¹ Figure A-2 shows the stress distribution in the fully plastic solid disk, scaled by the same factor used in Figure A-1. The tangential stress equals the yield

¹ Nadai, A. *Theory of Flow and Fracture of Solids*. Vol. 1, New York: McGraw-Hill Book Company, Inc., 1950.

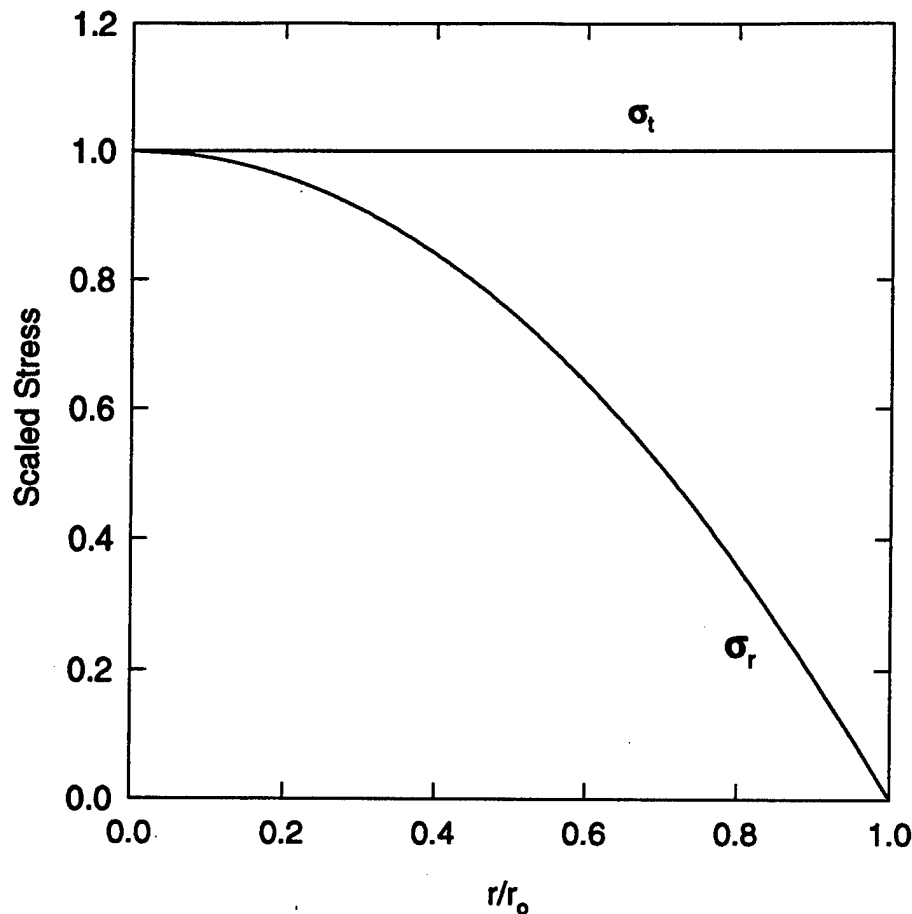


Figure A-2. Scaled Stresses in the Fully Plastic Spinning Solid Disk.

strength everywhere and the radial stress is determined from equation A-32. Thus, in terms of the angular velocity at which the entire disk has yielded, ω_f , the yield strength is given by:

$$\sigma_o = \frac{\rho r_o^2 \omega_f^2}{3}. \quad (\text{A-39})$$

2.2 Annular Disks

In the case of the annular rotating disk, as long as the stresses are below the yield point, they are given by equations A-23 and A-24. The annular disk first yields at the inner radius, $r = r_i$, at a peripheral speed v_{ca} that is determined by equating the tangential stress to σ_0 at r_i . From equation A-24

$$\sigma_0 = \frac{(3 + v)\rho\omega_{ca}^2}{8} \left(2r_o^2 + r_i^2 \left(1 - \frac{1 + 3v}{3 + v} \right) \right), \quad (\text{A-40})$$

so,

$$\rho\omega_{ca}^2 r_o^2 = \frac{4\sigma_0 r_o^2}{(3 + v)r_o^2 + (1 - v)r_i^2}. \quad (\text{A-41})$$

In terms of the reference peripheral velocity, $v_o^2 = \sigma_0/\rho$, v_{ca} is

$$v_{ca}^2 = \frac{4v_o^2 r_o^2}{(3 + v)r_o^2 + (1 - v)r_i^2}, \quad (\text{A-42})$$

which differs from Nadai's result¹ in which r_i^2 appears in the numerator rather than r_o^2 , apparently due to a typographical error. Note, that as r_i approaches zero, v_{ca} approaches one half of v_c , the critical peripheral speed for the onset of yielding for a solid disk (equation A-27). This is true because the tangential stress at the center of a solid disk (equation A-22) is half as large as the tangential stress on the inner radius of a disk with a central pinhole (equation A-24 with $r = r_i \approx 0$). The stresses for an annular disk with a ratio of $r_i/r_o = 1/5$, spinning at its critical speed for the onset of yielding, are shown in Figure A-3. The scaling factor is the same factor used previously but replacing ω_c^2 with

¹ Nadai, A. *Theory of Flow and Fracture of Solids*. Vol. 1, New York: McGraw-Hill Book Company, Inc., 1950.

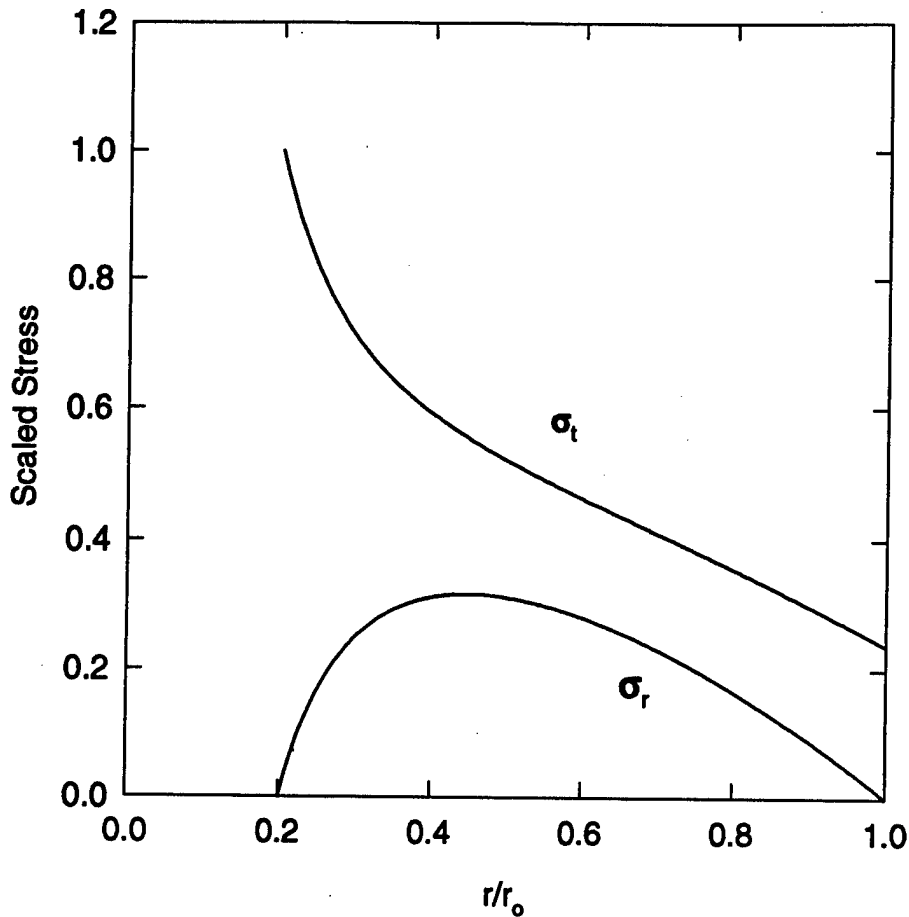


Figure A-3. Scaled Stresses in the Spinning Annular Disk at the Critical Velocity.

$$\omega_{ca}^2 = \frac{r_o^2}{2r_o^2 + r_i^2 \left(1 - \frac{1+3v}{3+v} \right)} \omega_c^2$$

obtained by setting equal the two expressions for σ_o , equations A-28 and A-40.

As the peripheral speed is increased, the boundary between the plastic inner region and the elastic outer region will move toward the outer radius of the disk. As in the case of the solid disk, the tangential stress is always larger than the radial stress, so the yield criterion gives

$$\sigma_t = \sigma_o \quad (A-43)$$

in the plastic region extending from $r = r_i$ to $r = r_p$. The radial stress is given by equation A-31, with the constant determined by the condition that at $r = r_i$, $\sigma_r = 0$. Thus,

$$\sigma_r = \sigma_o \left(1 - \frac{r_i}{r} \right) + \frac{\rho \omega^2}{3} \left(\frac{r_i^3}{r} - r^2 \right). \quad (A-44)$$

In the elastic region, extending from $r = r_p$ to $r = r_o$, the stresses are given by equations A-16 and A-17 subject to the boundary conditions that at $r = r_o$, $\sigma_r = 0$, and at $r = r_p$, σ_r is given by equation A-44. Applying the condition that $\sigma_r = 0$ at $r = r_o$ gives, from equation A-17,

$$C_1 = \frac{(3 + v)}{8} \rho \omega^2 r_o^2 - \frac{C_2}{r_o^2}. \quad (A-45)$$

Applying the condition that σ_r is given by equation A-44 when $r = r_p$ gives, from equation A-17,

$$C_2 = \frac{r_o^2 r_p}{r_o^2 - r_p^2} \left(\sigma_o (r_p - r_i) + \frac{\rho \omega^2 (r_i^3 - r_p^3)}{3} - \frac{(3 + v) \rho \omega^2 (r_o^2 r_p - r_p^3)}{8} \right). \quad (A-46)$$

Applying the condition that $\sigma_t = \sigma_o$ at $r = r_p$ gives, from equation A-16,

$$\omega^2 r_o^2 = \frac{12(\sigma_o/\rho)(2r_o^4 r_p - r_i r_o^2(r_o^2 + r_p^2))}{(3(3 + v)r_p r_o^4 - (1 + 3v)(2r_o^2 - r_p^2)r_p^3 - 4(r_o^2 + r_p^2)r_i^3)}. \quad (A-47)$$

This result differs from Nadai's¹ by a factor of (r_i^2/r_o^2) , which appears erroneously in his numerator. Johnson and Mellor² found that yielding first occurs when equation A-41 is satisfied, and they also found equation A-44 for the radial stress. Their equation for the elastic plastic boundary is incorrect, however, apparently because of a typographical error. The entire disk yields when $r_p = r_o$; equation A-47 then gives

$$\omega_f^2 r_o^2 = \frac{3(\sigma_o/\rho)(r_o - r_i)r_o^2}{r_o^3 - r_i^3}, \quad (A-48)$$

or, in terms of reference velocity v_o , the peripheral speed for the fully plastic annular disk is

$$v^2 = \frac{v_o^2 3 r_o^2}{r_i^2 + r_i r_o + r_o^2}. \quad (A-49)$$

This result also differs from Nadai's.¹ He has r_i^2 in the numerator instead of r_o^2 . In terms of v_o , $v = 1.56 v_o$, the peripheral speed at which the solid disk begins to yield at the center. Figure A-4 shows the tangential and radial stresses for the fully plastic annular disk, scaled by the same factor as used previously. The yield strength may be found by solving equation A-48 for σ_o ,

$$\sigma_o = \rho \omega^2 (r_i^2 + r_i r_o + r_o^2)/3. \quad (A-50)$$

This result can also be obtained by substituting $r = r_o$ in equation A-44 and setting the radial stress to zero. An expression equivalent to equation A-50 was also obtained by Robinson⁴ by defining the average bursting stress to be equal to the total centrifugal bursting force divided by the total

¹ Nadai, A. *Theory of Flow and Fracture of Solids*. Vol. 1, New York: McGraw-Hill Book Company, Inc., 1950.

² Johnson, W., and P. B. Mellor. *Engineering Plasticity*. New York: Van Nostrand Reinhold Company, 1973.

⁴ Robinson, E. L. "Bursting Tests of Steam-Turbine Disk Wheels." *Transactions of the ASME*, vol. 66, pp. 373-386, July 1944.

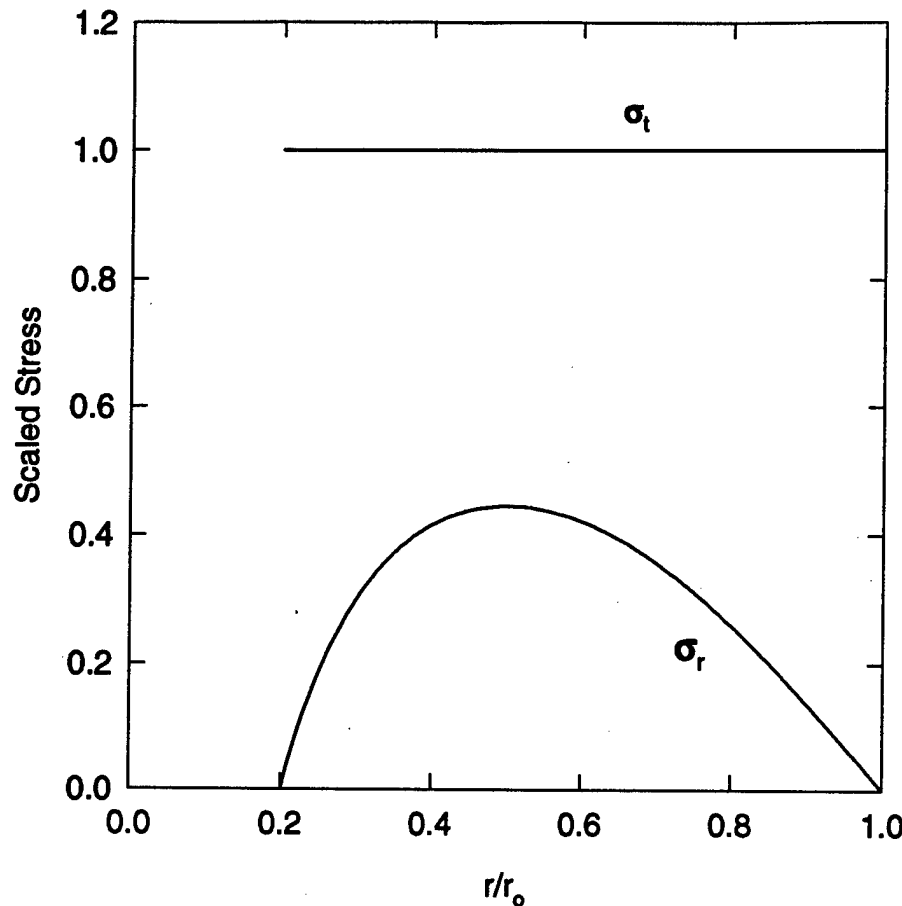


Figure A-4. Scaled Stresses in the Fully Plastic Spinning Annular Disk.

cross-sectional area. An experimental study, discussed in Johnson and Mellor,² showed that Robinson's criterion,⁴ when used to estimate the burst speed of a disk, was accurate to roughly $\pm 5\%$. In the limit as r_i approaches r_o , equation A-50 reduces to the result for a hoop,

$$\sigma_o = \rho \omega^2 r_o^2. \quad (\text{A-51})$$

² Johnson, W., and P. B. Mellor. *Engineering Plasticity*. New York: Van Nostrand Reinhold Company, 1973.

⁴ Robinson, E. L. "Bursting Tests of Steam-Turbine Disk Wheels." *Transactions of the ASME*, vol. 66, pp. 373-386, July 1944.

INTENTIONALLY LEFT BLANK.

Appendix B:

Stresses in Solid and Annular Cylinders

INTENTIONALLY LEFT BLANK.

In this appendix, the equations relating the yield strength of a material to the angular velocity that causes a long right-circular cylinder rotating about its axis to completely yield are derived. The plastic stress distributions in the cylinder are examined at the point where the cylinder becomes fully plastic. The stress distribution in a perfectly plastic, solid, rotating cylinder was examined by Nadai assuming small plastic strain and ignoring the elastic strain. Davis and Connelly¹ examined both the solid and annular cylinder and included the effect of strain hardening. Both Nadai² and Davis and Connelly¹ assumed the cylinder was rotating freely with no net axial force. Hodge and Balaban³ also analyzed the elastic plastic stress distributions in a solid rotating cylinder and examined the effect of elastic strains, compressibility, linear strain hardening, and finite plastic strains on the accuracy of the solution. The results of Hodge and Balaban³ indicated that the point at which the cylinder becomes fully plastic can be closely approximated using the approach outlined by Nadai.² The solution presented in this appendix follows the derivations of Davis and Connelly¹ and Nadai² with a perfectly plastic material model. In addition, the effect of a nonzero net axial force is also considered.

1. Stress Distribution in Perfectly Plastic Cylinders

1.1 Solid Cylinders

The stress distribution can be calculated for a segment of the rotating jet that is represented as a rotating cylinder. The solution derived in this appendix treats only a fully plastic cylinder rotating at equilibrium (with no radial acceleration). The strain in the axial direction (ϵ_z) is assumed to be a constant ($-\epsilon_0$). For an incompressible material, the sum of the strains must be zero.

$$\epsilon_r + \epsilon_t + \epsilon_z = 0, \quad (B-1)$$

¹ Davis, E. A., and F. M. Connelly. "Stress Distribution and Plastic Deformation in Rotating Cylinders of Strain-Hardening Material." *Trans. ASME, Journal of Applied Mechanics*, vol. 26, Series E, no. 1, pp. 25–30, March 1959.

² Nadai, A. *Theory of Flow and Fracture of Solids*. Vol. 1, New York: McGraw-Hill Book Company, Inc., 1950.

³ Hodge, P. G., Jr., and M. Balaban. "Elastic-Plastic Analysis of a Rotating Cylinder." *Int. J. Mech. Sci.*, vol. 4, pp. 465–476, 1962.

and, assuming small strains,

$$\frac{du}{dr} + \frac{u}{r} - \varepsilon_o = 0, \quad (B-2)$$

where u is the radial displacement, and ε_r and ε_t are the radial and tangential strains, respectively. Integrating equation B-2 gives for the radial displacement

$$u = \frac{\varepsilon_o r}{2} + \frac{C}{r}, \quad (B-3)$$

where C is a constant of integration. In a solid cylinder, C must be zero and, from the strain-displacement relations,

$$\varepsilon_r = \frac{du}{dr} = \frac{\varepsilon_o}{2}, \quad (B-4)$$

$$\varepsilon_t = \frac{u}{r} = \frac{\varepsilon_o}{2}. \quad (B-5)$$

Under the assumptions of steady, slow plastic flow and small strains, the strains may be related to the stresses by the equations:²

$$\varepsilon_r = \frac{1}{\phi} \left(\sigma_r - \frac{\sigma_t + \sigma_z}{2} \right), \quad (B-6)$$

² Nadai, A. *Theory of Flow and Fracture of Solids*. Vol. 1, New York: McGraw-Hill Book Company, Inc., 1950.

$$\varepsilon_t = \frac{1}{\phi} \left(\sigma_t - \frac{\sigma_r + \sigma_z}{2} \right), \quad (B-7)$$

$$\varepsilon_z = \frac{1}{\phi} \left(\sigma_z - \frac{\sigma_r + \sigma_t}{2} \right), \quad (B-8)$$

where ϕ is a variable to be determined. Since $\varepsilon_r = \varepsilon_t$, from equations B-6 and B-7 the radial and tangential stresses must also be equal. Therefore, the Tresca yield criterion is simply,

$$\sigma_t - \sigma_z = \pm \sigma_o = \text{constant}, \quad (B-9)$$

and the positive sign is assumed noting that if $\sigma_z > \sigma_t$ then σ_o will be negative.

The condition of equilibrium is

$$\frac{d\sigma_r}{dr} - \frac{\sigma_t - \sigma_r}{r} + \rho \omega^2 r = 0. \quad (B-10)$$

Substituting $\sigma_t = \sigma_r$ and integrating gives

$$\sigma_r = -\frac{\rho \omega^2 r^2}{2} + C_1, \quad (B-11)$$

and the condition that $\sigma_r = 0$ at $r = r_o$, the outside radius of the cylinder, requires that

$$C_1 = \frac{\rho \omega^2 r_o^2}{2}. \quad (B-12)$$

Therefore,

$$\sigma_r = \frac{\rho \omega^2 (r_o^2 - r^2)}{2}. \quad (\text{B-13})$$

The axial stress is given by

$$\sigma_z = \sigma_t - \sigma_o, \quad (\text{B-14})$$

or

$$\sigma_z = \frac{\rho \omega^2 (r_o^2 - r^2)}{2} - \sigma_o. \quad (\text{B-15})$$

In a freely rotating cylinder, which can contract freely in the axial direction, the resultant of the axial stresses σ_z is zero,

$$\int_0^{r_o} 2\pi \sigma_z r dr = 0, \quad (\text{B-16})$$

and the result of the integration is

$$\sigma_o = \rho \omega^2 r_o^2 / 4. \quad (\text{B-17})$$

In terms of the peripheral speed at which the entire cylinder will yield,

$$v^2 = (r_o \omega)^2 = 4 (\sigma_o / \rho) = 4 v_o^2, \quad (\text{B-18})$$

or

$$v = 2 v_o. \quad (\text{B-19})$$

The result for the solid disk was $v = 1.73 v_o$. For the same value of v , the estimated yield strength is larger, $\rho v^2 / 3$ (equation A-39), for the solid disk in plane stress than for the solid cylinder in plane strain, $\rho v^2 / 4$.

When the entire rotating solid cylinder becomes fully plastic, the stress distributions are

$$\begin{aligned}\sigma_r = \sigma_t &= \frac{\rho \omega^2 r_o^2}{2} \left(1 - \frac{r^2}{r_o^2} \right), \\ &= 2\sigma_o \left(1 - \frac{r^2}{r_o^2} \right),\end{aligned}\quad (\text{B-20})$$

and

$$\sigma_z = \sigma_t - \sigma_o = \sigma_o \left(1 - 2 \frac{r^2}{r_o^2} \right). \quad (\text{B-21})$$

In the axial direction, the stress is tensile from $r = 0$ to nearly $r = 0.707r_o$ and compressive from there to the periphery. The action of the compressive and tensile forces is balanced so that the resultant force is zero. All of the above results were obtained by Nadai.²

When there is a net axial force T acting on the cylinder

$$\int_0^{r_o} 2\pi\sigma_z r dr = T, \quad (\text{B-22})$$

the expression for the yield strength becomes

$$\sigma_o = \frac{\rho \omega^2 r_o^2}{4} - \frac{T}{\pi r_o^2} \quad (\text{B-23})$$

and

$$v^2 = \omega^2 r_o^2 = \frac{4}{\rho} \left(\sigma_o + \frac{T}{\pi r_o^2} \right).$$

² Nadai, A. *Theory of Flow and Fracture of Solids*. Vol. 1, New York: McGraw-Hill Book Company, Inc., 1950.

If T is positive, the tension increases the peripheral speed necessary to cause the entire cylinder to yield. Therefore, at a given value of peripheral speed, v , the material may not yield until the tension is released by "breaking" the cylinder. Conversely, if T is negative, the compression reduces the peripheral speed necessary to cause yielding. In this report, the yield strength is unknown and is determined based upon measurement of the critical spin rate or peripheral speed at which the jet material accelerates radially (bursts). Thus, a cylinder under a net axial tension will appear to have a higher yield strength than a cylinder under no net axial force or under compression.

1.2 Annular Cylinders

In the case of the annular cylinder, the constant C in equation B-3 is not required to vanish, and the strains become

$$\varepsilon_r = \frac{\varepsilon_o}{2} - \frac{C}{r^2}, \quad (B-24)$$

$$\varepsilon_t = \frac{\varepsilon_o}{2} + \frac{C}{r^2}, \quad (B-25)$$

and

$$\varepsilon_z = -\varepsilon_o. \quad (B-26)$$

The stresses and strains are related by equations B-6, B-7, and B-8, so, from the previous equations, the principal stress differences are

$$\sigma_t - \sigma_r = \frac{4C\phi}{3r^2} = \frac{2\phi\varepsilon_0 k^2}{r^2}, \quad (B-27)$$

$$\sigma_r - \sigma_z = \phi \left(\epsilon_o - \frac{2C}{3r^2} \right) = \frac{\phi \epsilon_o (r^2 - k^2)}{r^2}, \quad (B-28)$$

and

$$\sigma_t - \sigma_z = \phi \left(\epsilon_o + \frac{2C}{3r^2} \right) = \frac{\phi \epsilon_o (r^2 + k^2)}{r^2}, \quad (B-29)$$

where

$$k^2 = 2C / 3\epsilon_o. \quad (B-30)$$

The equation of equilibrium is

$$\frac{d\sigma_r}{dr} = \frac{\sigma_t - \sigma_r}{r} - \rho \omega^2 r. \quad (B-31)$$

Examination of equations B-27, B-28, and B-29 reveals that the Tresca yield criterion results in two regions in the annular cylinder. For $r < k$, $\sigma_o = \pm(\sigma_t - \sigma_r)$. For $r > k$, $\sigma_o = \pm(\sigma_t - \sigma_z)$. In the case of a freely rotating cylinder, the tangential stress is positive and is always greater than both the axial and radial stresses. At $r = r_i$, the inner radius of the cylinder, the axial stress is also tensile and the radial stress is zero; therefore, the magnitudes of the stresses are $\sigma_t > \sigma_z > \sigma_r$. The yield condition is then $\sigma_t - \sigma_r = \sigma_o$, and integration of equation B-31 yields

$$\sigma_r = \sigma_o \ln(r) - \frac{\rho \omega^2 r^2}{2} + C_2. \quad (B-32)$$

This equation has a single constant, which is used to satisfy the condition that $\sigma_r = 0$ at $r = r_i$. The constant C_2 is

$$C_2 = \frac{\rho \omega^2 r_i^2}{2} - \sigma_o \ln(r_i). \quad (B-33)$$

When the net axial force is zero, σ_z is in tension near the center of the cylinder and in compression (negative) near the outside of the cylinder, so it will drop below σ_r in the outer region of the cylinder. In the inner region, $r < k$, the yielding is governed by the difference between the tangential and radial stresses, while in the outer region, it is governed by the difference between the tangential and the axial stresses. Thus,

$$\sigma_o = \sigma_t - \sigma_r \quad r_i \leq r \leq k, \quad (B-34)$$

and

$$\sigma_o = \sigma_t - \sigma_z \quad k \leq r \leq r_o. \quad (B-35)$$

From equations B-27 and B-34,

$$\phi = \frac{\sigma_o r^2}{2\epsilon_o k^2} \quad (B-36)$$

in the inner region, and from equations B-29 and B-35,

$$\phi = \frac{\sigma_o r^2}{\epsilon_o (r^2 + k^2)} \quad (B-37)$$

for $k \leq r \leq r_o$.

In the outer region,

$$\begin{aligned} \sigma_t - \sigma_r &= (\sigma_o + \sigma_z) - \sigma_r, \\ &= \sigma_o - \frac{\phi \epsilon_o (r^2 - k^2)}{r^2}. \end{aligned} \quad (B-38)$$

The equilibrium equation in the outer region becomes

$$\frac{d\sigma_r}{dr} = \frac{\sigma_o}{r} - \frac{\phi \epsilon_o (r^2 - k^2)}{r^3} - \rho \omega^2 r. \quad (B-39)$$

Substituting for ϕ gives

$$\frac{d\sigma_r}{dr} = \frac{\sigma_o}{r} \left(1 - \frac{(r^2 - k^2)}{(r^2 + k^2)} \right) - \rho \omega^2 r. \quad (B-40)$$

On integration by partial fractions (or integral tables),

$$\sigma_r = \sigma_o \ln \left(\frac{r^2}{r^2 + k^2} \right) - \frac{\rho \omega^2 r^2}{2} + C_3, \quad (B-41)$$

where C_3 is the constant of integration and k is the (unknown) transition point.

The solutions for σ_r must match at $r = k$, so from equations B-32 and B-41,

$$C_3 - C_2 = \sigma_o \ln (2k). \quad (B-42)$$

Thus,

$$C_3 = \sigma_o \ln \left(\frac{2k}{r_i} \right) + \frac{\rho \omega^2 r_i^2}{2}. \quad (B-43)$$

But σ_r must vanish at $r = r_o$, so

$$C_3 = \frac{\rho \omega^2 r_o^2}{2} - \sigma_o \ln \left(\frac{r_o^2}{r_o^2 + k^2} \right). \quad (B-44)$$

Setting these two expressions for C_3 equal gives an equation for k , namely,

$$\ln\left(\frac{2kr_o^2}{r_i(r_o^2 + k^2)}\right) = \frac{\rho\omega^2(r_o^2 - r_i^2)}{2\sigma_o} \quad (B-45)$$

or

$$\frac{k}{(r_o^2 + k^2)} = \frac{r_i}{2r_o^2} \exp\left(\frac{\rho\omega^2(r_o^2 - r_i^2)}{2\sigma_o}\right).$$

If one defines

$$A = \frac{r_i}{2r_o^2} \exp\left(\frac{\rho\omega^2(r_o^2 - r_i^2)}{2\sigma_o}\right), \quad (B-46)$$

then

$$k = \frac{1 \pm \sqrt{1 - 4A^2r_o^2}}{2A}. \quad (B-47)$$

From equation B-47, k can be found in terms of σ_o . From the condition on the net axial force

$$F = \int_{r_i}^{r_o} 2\pi\sigma_z r dr, \quad (B-48)$$

another equation linking k and σ_o is generated. Equations B-47 and B-48 are solved iteratively for σ_o and k .

Summarizing the stress equations in the inner region

$$\sigma_r = \sigma_o \ln(r) - \frac{\rho \omega^2 r^2}{2} + \frac{\rho \omega^2 r_i^2}{2} - \sigma_o \ln(r_i), \quad (B-49)$$

$$\sigma_t = \sigma_r + \sigma_o, \quad (B-50)$$

and

$$\sigma_z = \sigma_r - \frac{\sigma_o(r^2 - k^2)}{2k^2}, \quad (B-51)$$

while in the outer region

$$\sigma_r = \sigma_o \ln\left(\frac{r^2}{r^2 + k^2}\right) - \frac{\rho \omega^2 r^2}{2} + \frac{\rho \omega^2 r_o^2}{2} - \sigma_o \ln\left(\frac{r_o^2}{r_o^2 + k^2}\right), \quad (B-52)$$

$$\sigma_t = \sigma_z + \sigma_o = \sigma_r + \frac{2\sigma_o k^2}{r^2 + k^2}, \quad (B-53)$$

and

$$\sigma_z = \sigma_r - \sigma_o \left(\frac{r^2 - k^2}{r^2 + k^2} \right). \quad (B-54)$$

The stresses for the fully plastic annular cylinder, scaled by the yield strength, for the ratio of $r_i/r_o = 1/5$ are shown in Figure B-1.

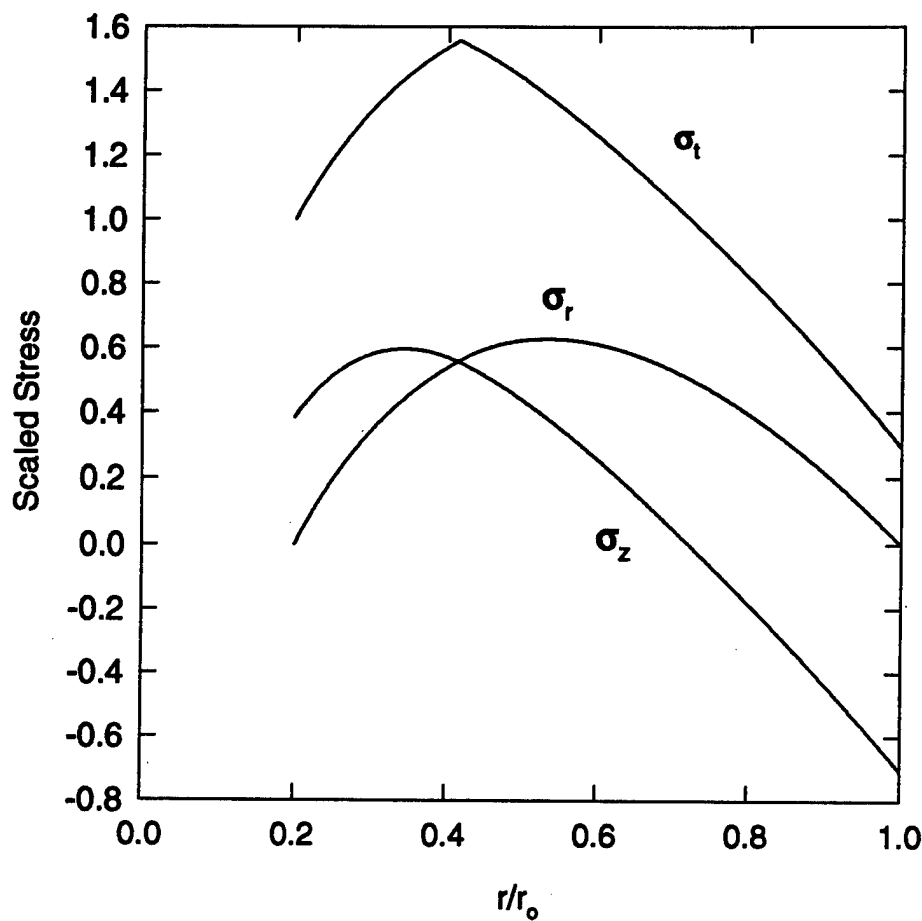


Figure B-1. Scaled Stresses in the Fully Plastic Spinning Annular Cylinder.

Appendix C:
Computed Jet Characteristics

INTENTIONALLY LEFT BLANK.

In this appendix, the calculation of the spin rate of a jet element is described. This method differs from the one used by Karpp and Simon,¹ who separated the portion of the liner that becomes the jet from the rest of the liner at the start of the collapse process. In the method described here, the jet is divided from the rest of the liner at the start of the jet-formation process (see Figure 9).

The spin rate of the jet elements was computed from the initial spin rate of the liner in the following manner. The conical portion of the liner, beginning immediately after the spherical nose cap, was divided into 100-ring segments. The moment of inertia of segment i (I_{oi}) having inner radius R_{1i} and outer radius R_{2i} is given by

$$I_{oi} = M_i (R_{1i}^2 + R_{2i}^2)/2 , \quad (C-1)$$

where the mass M_i is

$$M_i = \pi \rho (R_{2i}^2 - R_{1i}^2) \Delta z , \quad (C-2)$$

and the length of the ring is Δz .

As shown in the collapse sequence diagram (Figure 9), the liner segment collapses to a certain position at which it begins to divide into a jet and a slug portion. The radii of the ring (R_{1Ci} and R_{2Ci}) are evaluated at this point, and a new moment of inertia (I_{Ci}) is calculated from equation C-3:

$$I_{Ci} = M_i (R_{1Ci}^2 + R_{2Ci}^2)/2 . \quad (C-3)$$

A new spin rate for the ring at the collapse position (ω_{Ci}) is computed from equation C-4:

$$\omega_{Ci} = \omega_1 = I_{oi} \omega_o / I_{Ci} , \quad (C-4)$$

¹ Karpp, R. R., and J. Simon. "An Estimate of the Strength of a Copper Shaped Charge Jet and the Effect of Strength on the Breakup of a Stretching Jet." BRL-TR-1893, U.S. Army Ballistic Research Laboratory, Aberdeen Proving Ground, MD, June 1976.

where ω_0 is the initial spin rate of the liner. The assumption is made that the effect of torques transmitted by neighboring rings can be neglected.

The division of the ring mass into a jet mass (m_i) and a slug mass ($M_i - m_i$) is governed by the collapse angle (β) according to equation C-5:²

$$m_i = M_i \sin^2(\beta/2), \quad (C-5)$$

where β is the angle made by the line connecting the outer radii of the rings labeled i and $i + 1$, and the z axis. Since the masses are proportional to the lateral areas of the rings, once m_i is known, the radius to the upper surface of the jet ring can be found, namely,

$$R_{3Ci} = (R_{2Ci}^2 \sin^2(\beta/2) + R_{1Ci}^2 \cos^2(\beta/2))^{1/2}. \quad (C-6)$$

The moment of inertia of the jet element at this time (I_{Cji}) is given by

$$I_{Cji} = m_i (R_{1Ci}^2 + R_{3Ci}^2)/2. \quad (C-7)$$

The jet element continues to collapse onto the axis of symmetry. This as-formed jet is assumed to be solid, with a radius determined by its mass, namely,

$$\begin{aligned} r_{ji} &= (m_i / \pi \rho \Delta z)^{1/2}, \\ &= ((R_{2Ci}^2 - R_{1Ci}^2) \sin^2(\beta/2))^{1/2}, \end{aligned} \quad (C-8)$$

where ρ is the mass density of the liner. The moment of inertia of the jet is then

$$I_{ji} = m_i r_{ji}^2/2, \quad (C-9)$$

² Harrison, J. T. "Improved Analytical Shaped Charge Code: BASC." BRL-TR-02300, U.S. Army Ballistic Research Laboratory, Aberdeen Proving Ground, MD, March 1981.

and the as-formed spin rate follows from equation C-10:

$$\omega_{ji} = \omega_2 = I_{Cji} \omega_{Ci} / I_{ji} . \quad (C-10)$$

The as-formed jet segments have smaller radii than the jet segments observed in the radiographs. After formation, the jet segments at the front of the pellet are compressed by the strong "inverse" velocity gradient and, consequently, change their shapes. At the rear of the pellet, the compressive stresses are lower and the discrepancy between the as-formed and the observed segment radius is much less. Consequently, after formation, the jet segments are assumed to "relax" to a ring whose outer radius is that measured from the radiographs. The moment of inertia of this ring (I_{ji}) is given by

$$I_{ji} = m_i (r_{1i}^2 + r_{2i}^2)/2 , \quad (C-11)$$

where r_2 is the outer (observed) jet radius and r_{1i} is determined by the mass of the jet ring. The spin rate in the relaxed state (ω_i) is computed from equation C-12:

$$\omega_i = \omega_3 = I_{Cji} \omega_{Ci} / I_{ji} . \quad (C-12)$$

The jet pellet reaches an equilibrium value of velocity. This velocity, \bar{v} , is determined by conservation of linear momentum as given by equation C-13:

$$\bar{v} = \sum (m_i v_i) / \sum m_i \quad v_i > \bar{v} , \quad (C-13)$$

where the sums are taken over all those jet segments that can overtake one another. Elements 1–63 comprise the pellet; its velocity is 10,433 m/s.

Table C-1 gives some computed jet properties obtained from the modified BASC code. For a given liner segment number (N), beginning near the apex, these are the segment jet velocity (V_j), the mass of the jet segment (m), the radius of the as-formed jet segment (r_j), the collapse velocity (V_c)

Table C-1. Computed Jet Properties

N	V _j (km/s)	m (kg)	r _j (mm)	V _o (km/s)	β (deg)	ω _o (rev/s)	ω ₂ (rev/s)
1	9.393	9.1×10^{-5}	1.47	2.481	31.7	42/60	2586/3694
2	9.489	9.6×10^{-5}	1.51	2.528	32.0	42/60	2634/3762
3	9.536	1.0×10^{-4}	1.56	2.570	32.4	42/60	2662/3803
4	9.616	1.1×10^{-4}	1.60	2.609	32.6	42/60	2715/3878
5	9.647	1.1×10^{-4}	1.64	2.644	33.0	42/60	2747/3925
6	9.712	1.2×10^{-4}	1.67	2.675	33.2	42/60	2805/4007
7	9.731	1.2×10^{-4}	1.72	2.704	33.5	42/60	2842/4059
8	9.855	1.3×10^{-4}	1.73	2.730	33.4	42/60	2946/4208
9	9.929	1.3×10^{-4}	1.76	2.758	33.5	42/60	3016/4309
10	9.976	1.4×10^{-4}	1.80	2.786	33.7	42/60	3067/4381
11	9.977	1.4×10^{-4}	1.84	2.812	34.0	42/60	3091/4416
12	10.016	1.5×10^{-4}	1.88	2.813	34.2	42/60	3144/4492
13	10.054	1.5×10^{-4}	1.91	2.860	34.4	42/60	3196/4566
14	10.087	1.6×10^{-4}	1.94	2.881	34.5	42/60	3250/4643
15	10.119	1.6×10^{-4}	1.97	2.901	34.7	42/60	3305/4722
16	10.148	1.7×10^{-4}	2.00	2.920	34.8	42/60	3361/4801
17	10.175	1.7×10^{-4}	2.04	2.938	34.9	42/60	3417/4881
18	10.201	1.8×10^{-4}	2.07	2.955	35.1	42/60	3473/4962
19	10.225	1.8×10^{-4}	2.10	2.970	35.2	42/60	3530/5043
20	10.248	1.9×10^{-4}	2.12	2.985	35.3	42/60	3588/5126
21	10.269	1.9×10^{-4}	2.15	2.999	35.4	42/60	3646/5209
22	10.289	2.0×10^{-4}	2.18	3.012	35.5	42/60	3704/5291
23	10.307	2.1×10^{-4}	2.21	3.024	35.6	42/60	3763/5376
24	10.325	2.1×10^{-4}	2.24	3.036	35.6	42/60	3822/5461
25	10.385	2.1×10^{-4}	2.25	3.047	35.6	42/60	3919/5598
26	10.400	2.2×10^{-4}	2.28	3.057	35.6	42/60	3980/5685
27	10.415	2.2×10^{-4}	2.30	3.067	35.7	42/60	4041/5772
28	10.428	2.3×10^{-4}	2.33	3.076	35.8	42/60	4102/5860
29	10.440	2.3×10^{-4}	2.36	3.084	35.8	42/60	4165/5950
30	10.453	2.4×10^{-4}	2.38	3.092	35.9	42/60	4228/6040
31	10.464	2.4×10^{-4}	2.40	3.100	35.9	42/60	4290/6129
32	10.474	2.5×10^{-4}	2.43	3.107	36.0	42/60	4353/6218
33	10.484	2.5×10^{-4}	2.45	3.114	36.0	42/60	4415/6308
34	10.494	2.6×10^{-4}	2.48	3.121	36.1	42/60	4479/6398
35	10.502	2.6×10^{-4}	2.50	3.127	36.1	42/60	4544/6492
36	10.510	2.7×10^{-4}	2.52	3.132	36.2	42/60	4608/6583
37	10.519	2.7×10^{-4}	2.55	3.138	36.2	42/60	4672/6675
38	10.526	2.8×10^{-4}	2.57	3.143	36.3	42/60	4736/6766
39	10.534	2.8×10^{-4}	2.59	3.148	36.3	42/60	4802/6859

Table C-1. Computed Jet Properties (continued)

N	V _j (km/s)	m (kg)	r _j (mm)	V _o (km/s)	β (deg)	ω _o (rev/s)	ω ₂ (rev/s)
40	10.540	2.9×10^{-4}	2.61	3.153	36.3	42/60	4866/6952
41	10.545	2.9×10^{-4}	2.63	3.157	36.4	42/60	4930/7043
42	10.552	3.0×10^{-4}	2.66	3.161	36.4	42/60	4996/7137
43	10.558	3.0×10^{-4}	2.68	3.165	36.4	42/60	5062/7231
44	10.563	3.1×10^{-4}	2.70	3.169	36.4	42/60	5127/7325
45	10.568	3.1×10^{-4}	2.72	3.173	36.5	42/60	5193/7418
46	10.573	3.2×10^{-4}	2.74	3.176	36.5	42/60	5259/7512
47	10.578	3.2×10^{-4}	2.76	3.180	36.5	42/60	5325/7608
48	10.581	3.3×10^{-4}	2.78	3.183	36.6	42/60	5390/7700
49	10.585	3.3×10^{-4}	2.80	3.186	36.6	42/60	5457/7795
50	10.589	3.3×10^{-4}	2.82	3.189	36.6	42/60	5523/7890
51	10.589	3.3×10^{-4}	2.84	3.192	36.6	42/60	5589/7985
52	10.597	3.4×10^{-4}	2.86	3.194	36.6	42/60	5656/8081
53	10.600	3.5×10^{-4}	2.88	3.197	36.7	42/60	5723/8175
54	10.602	3.5×10^{-4}	2.90	3.199	36.7	42/60	5788/8269
55	10.605	3.6×10^{-4}	2.92	3.202	36.7	42/60	5855/8365
56	10.609	3.6×10^{-4}	2.94	3.204	36.7	42/60	5920/8458
57	10.613	3.7×10^{-4}	2.96	3.206	36.7	42/60	5989/8555
58	10.616	3.7×10^{-4}	2.98	3.208	36.7	42/60	6057/8653
59	10.615	3.8×10^{-4}	3.00	3.210	36.8	42/60	6120/8743
60	10.619	3.8×10^{-4}	3.01	3.212	36.8	42/60	6188/8841
61	10.622	3.9×10^{-4}	3.03	3.214	36.8	42/60	6257/8938
62	10.626	3.9×10^{-4}	3.05	3.216	36.8	42/60	6322/9032
63	10.569	4.0×10^{-4}	3.09	3.218	37.0	42/60	6316/9023
64	10.012	4.6×10^{-4}	3.30	3.219	39.4	42/60	5698/8140
65	9.996	4.6×10^{-4}	3.31	3.208	39.4	42/60	5779/8256
66	9.981	4.6×10^{-4}	3.32	3.198	39.3	42/60	5861/8373
67	9.917	4.7×10^{-4}	3.35	3.187	39.4	42/60	5887/8410
68	9.900	4.8×10^{-4}	3.36	3.176	39.3	42/60	5966/8523
69	9.843	4.8×10^{-4}	3.39	3.165	39.4	42/60	5999/8569
70	9.825	4.9×10^{-4}	3.40	3.154	39.4	42/60	6083/8691
71	9.673	5.0×10^{-4}	3.46	3.142	39.9	42/60	5994/8563
72	8.252	7.1×10^{-4}	4.12	3.129	47.6	42/60	4407/6295
73	8.037	7.4×10^{-4}	4.19	3.084	48.3	42/60	4343/6205
74	7.820	7.7×10^{-4}	4.27	3.038	49.0	42/60	4280/6115
75	7.595	7.9×10^{-4}	4.35	2.988	49.7	42/60	4212/6018
76	7.360	8.3×10^{-4}	4.43	2.936	50.5	42/60	4135/5908
77	7.111	8.6×10^{-4}	4.53	2.882	51.4	42/60	4048/5782
78	6.789	9.2×10^{-4}	4.68	2.825	52.9	42/60	3882/5547
79	6.572	9.5×10^{-4}	4.75	2.765	53.5	42/60	3837/5481
80	6.228	1.0×10^{-3}	4.93	2.702	55.4	42/60	3653/5219

of the liner segment, the collapse angle (β) of the liner segment, the initial spin rate (ω_0) of the liner segment, either 42 rps or 60 rps, and the corresponding as-formed jet spin rate, ω_2 .

If the hoop model, used by Karpp and Simon¹ is used to calculate the spin rate of the jet element formed from a liner element initially located at r_{oi} , the result will differ from that computed by the procedure outlined above. If r_g is the radius of gyration of the jet, the jet spin rate computed from

$$(\omega_{ji} / \omega_0) = (r_{oi} / r_g)^2 \quad (C-14)$$

is higher because the jet mass is split off from the rest of the liner mass in the initial state before the collapse begins, and the initial moment of inertia about the z axis (I_{oi}^{hoop}) is

$$I_{oi}^{hoop} = m_i r_{oi}^2, \quad (C-15)$$

where m_i is the mass of the jet element and r_{oi} is its initial location on the inside surface of the liner. The jet-formation code, using the ring model (Figure 9), evaluates an intermediate state between the initial and final states and uses the moment of inertia of the entire liner segment at the initial and intermediate points. The final states of the jet element can be compared if the radius of the hoop is set equal to the radius of gyration (r_g) of the solid disk representing the solid jet, given by

$$r_g = \sqrt{\frac{r^2}{2}}, \quad (C-16)$$

where r is the radius of the jet. The radius of gyration of a hollow jet, with outer radius r_1 and inner radius r_2 is

$$r_g = \sqrt{\frac{r_1^2 + r_2^2}{2}}.$$

¹ Karpp, R. R., and J. Simon. "An Estimate of the Strength of a Copper Shaped Charge Jet and the Effect of Strength on the Breakup of a Stretching Jet." BRL-TR-1893, U.S. Army Ballistic Research Laboratory, Aberdeen Proving Ground, MD, June 1976.

For example, using liner element 64 and the data in Table 2, the values for the quantities are: $r_o = R_1 = 31.1$ mm, $R_2 = 32.6$ mm, $R_{C1} = 10.1$ mm, $R_{C2} = 13.8$ mm, $R_{C3} = 10.6$ mm, and $r_j = 3.3$ mm. For $\omega_o = 42$ rps, the as-formed jet spin rate is 5,700 rps and the as-formed radius of gyration is 2.3 mm. Taking the outer radius to be 2.7 mm and the inner radius to be 1.3 mm, the radius of gyration at burst is 2.1 mm, smaller due to the subsequent stretch (see the discussion in section 6). This increases the as-formed spin rate from 5,700 to 6,800 rps so that $r_g^2 \omega$ remains constant. For $\omega_o = 60$ rps, the as-formed spin rate and radius of gyration are 8,100 rps and 2.3 mm. The radius of gyration at burst is 2.8 mm because the jet is assumed to expand before failing to an outer radius of 3.65 mm and an inner radius of 1.49 mm, equal to the observed outer radius at this part of the jet in the experiment at 42 rps. This reduces the spin rate from 8,100 to 5,500 rps. Using the hoop equation (C-14), the corresponding jet spin rates at burst are 9,200 and 7,400 rps. The fly-off velocity (v_{fo}) is the tangential velocity at the radius of gyration. The results of the two models are given in Table C-2. The jet-formation calculations using the disk model are expected to be more accurate than those using the hoop model, as the table shows, if the tangential velocity is given accurately by half the diametrical expansion rate.

Table C-2. Comparison of the Models for Liner Element 64

ω_o (rps)	r_g (mm)	ω_j^{hoop} (rps)	ω_j^{disk} (rps)	v_{fo}^{hoop} (m/s)	v_{fo}^{disk} (m/s)	$\frac{1}{2} dD/dt$ (m/s)
42	2.0	9,200	6,800	121	90	90 \pm 14
60	2.8	7,400	5,500	130	97	115 \pm 17

INTENTIONALLY LEFT BLANK.

<u>NO. OF COPIES</u>	<u>ORGANIZATION</u>	<u>NO. OF COPIES</u>	<u>ORGANIZATION</u>
2	DEFENSE TECHNICAL INFORMATION CENTER DTIC DDA 8725 JOHN J KINGMAN RD STE 0944 FT BELVOIR VA 22060-6218	1	INST FOR ADVNCED TCHNLGY THE UNIV OF TEXAS AT AUSTIN PO BOX 202797 AUSTIN TX 78720-2797
1	HQDA DAMO FDQ DENNIS SCHMIDT 400 ARMY PENTAGON WASHINGTON DC 20310-0460	1	USAASA MOAS AI W PARRON 9325 GUNSTON RD STE N319 FT BELVOIR VA 22060-5582
1	DPTY ASSIST SCY FOR R&T SARD TT F MILTON RM 3EA79 THE PENTAGON WASHINGTON DC 20310-0103	1	CECOM PM GPS COL S YOUNG FT MONMOUTH NJ 07703
1	OSD OUSD(A&T)/ODDDR&E(R) J LUPO THE PENTAGON WASHINGTON DC 20301-7100	1	GPS JOINT PROG OFC DIR COL J CLAY 2435 VELA WAY STE 1613 LOS ANGELES AFB CA 90245-5500
1	CECOM SP & TRRSTRL COMMCTN DIV AMSEL RD ST MC M H SOICHER FT MONMOUTH NJ 07703-5203	1	ELECTRONIC SYS DIV DIR CECOM RDEC J NIEMELA FT MONMOUTH NJ 07703
1	PRIN DPTY FOR TCHNLGY HQ US ARMY MATCOM AMCDCG T M FISETTE 5001 EISENHOWER AVE ALEXANDRIA VA 22333-0001	3	DARPA L STOTTS J PENNELLA B KASPAR 3701 N FAIRFAX DR ARLINGTON VA 22203-1714
1	PRIN DPTY FOR ACQSTN HQ US ARMY MATCOM AMCDCG A D ADAMS 5001 EISENHOWER AVE ALEXANDRIA VA 22333-0001	1	US MILITARY ACADEMY MATH SCI CTR OF EXCELLENCE DEPT OF MATHEMATICAL SCI MDN A MAJ DON ENGEN THAYER HALL WEST POINT NY 10996-1786
1	DPTY CG FOR RDE HQ US ARMY MATCOM AMCRD BG BEAUCHAMP 5001 EISENHOWER AVE ALEXANDRIA VA 22333-0001	1	DIRECTOR US ARMY RESEARCH LAB AMSRL CS AL TP 2800 POWDER MILL RD ADELPHI MD 20783-1145
		1	DIRECTOR US ARMY RESEARCH LAB AMSRL CS AL TA 2800 POWDER MILL RD ADELPHI MD 20783-1145

NO. OF
COPIES ORGANIZATION

3 DIRECTOR
US ARMY RESEARCH LAB
AMSRL CI LL
2800 POWDER MILL RD
ADELPHI MD 20783-1145

ABERDEEN PROVING GROUND

4 DIR USARL
AMSRL CI LP (305)

<u>NO. OF COPIES</u>	<u>ORGANIZATION</u>	<u>NO. OF COPIES</u>	<u>ORGANIZATION</u>
1	US ARMY ARDEC AMSTA AR AEE W R FONG BLDG 3022 PICATINNY ARSENAL NJ 07806-5002	1	US AIR FORCE WRIGHT LAB WRIGHT LAB/MUNITIONS DIRECT WL/MNMW J FOSTER JR EGLIN AFB FL 32548
1	US ARMY ARDEC AMSTA AR AEE W E BAKER BLDG 3022 PICATINNY ARSENAL NJ 07806-5000	1	DIRECTOR SANDIA NATL LABS M KIPP DIV 1533 PO BOX 5800 ALBUQUERQUE NM 87185
1	US ARMY MICOM AMSMI RD ST WF J COLE REDSTONE ARSENAL AL 35898-0001	1	LOS ALAMOS NATIONAL LAB L HULL DX 13 MS P940 PO BOX 1663 LOS ALAMOS NM 87544-0600
2	US ARMY MICOM AMSMI RD ST WF P TURNER S HILL REDSTONE ARSENAL AL 35898-5240	2	LAWRENCE LIVERMORE NATL LAB M MURPHY L 282 C SIMONSON L 170 PO BOX 808 LIVERMORE CA 94550
2	US ARMY MICOM AMSMI RD ST WF S HOWARD D LOVELACE REDSTONE ARSENAL AL 35898-5247	1	AEROJET J CARLEONE PO BOX 13222 SACRAMENTO CA 95813-6000
1	NAVAL SURFACE WARFARE CTR S WAGGENER G 22 17320 DAHLGREN ROAD DAHLGREN VA 22448-5150	2	DYNA EAST CORPORATION W FLIS R CICCARELLI 3620 HORIZON DRIVE KING OF PRUSSIA PA 19406-2647
1	NAVAL EOD TECHNOLOGY DIV CODE 50 J DELANEY 2008 STUMP NECK ROAD INDIAN HEAD MD 20640	1	TRACOR AEROSPACE INC MINE COUNTMEASURES DIVISION R BROWN 18124 BOLLINGER CANYON RD PO BOX 196 SAN RAMON CA 94583

<u>NO. OF COPIES</u>	<u>ORGANIZATION</u>	<u>NO. OF COPIES</u>	<u>ORGANIZATION</u>
1	FUTRON CORPORATION M CHAWLA 7315 WISCONSIN AVE STE 900W BETHESDA MD 20814-3202	1	SAIC A TOEPPER DIV 235 2109 AIR PARK ROAD SE ALBUQUERQUE NM 87106-3258
1	ENIG ASSOCIATES INC J ENIG 11120 NEW HAMPSHIRE AVE STE 500 SILVER SPRING MD 20904-2633	1	ZERNOW TECHNICAL SERVICES INC L ZERNOW 425 WEST BONITA AVE STE 208 SAN DIMAS CA 91773-2542
1	PRIMEX TECHNOLOGIES T GRAHAM 2700 MERCED STREET SAN LEANDRO CA 94577-0599	1	UNIV OF MARYLAND DEPT OF MECH ENGNR R ARMSTRONG COLLEGE PARK MD 20742
1	ALLIANT TECHSYSTEMS INC G JOHNSON MN11 1614 600 SECOND STREET NE HOPKINS MN 55343-8367		<u>ABERDEEN PROVING GROUND</u>
1	D R KENNEDY AND ASSOC INC D KENNEDY 745 DISTEL DRIVE STE 21 LOS ALTOS CA 94022-1523	24	DIR USARL AMSRL WM TC W DE ROSSET W WALTERS M LAMPSON R SUMMERS R MUDD E KENNEDY I GRACE L MAGNESS K KIMSEY AMSRL WM TB R FREY P BAKER AMSRL WM TD D DIETRICH K FRANK S SEGLETES T FARRAND S SCHOENFELD M RAFTENBERG A RAJENDRAN D DANDEKAR D PRITCHARD AMSRL WM TA D KLEPONIS M KEELE H MEYER G FILBEY
1	TRACOR AEROSPACE INC MCM DIVISION M MAJERUS 1400 PEOPLES PLAZA STE 233 NEWARK DE 19702-5707		
1	ORLANDO TECHNOLOGY INC D MATUSKA 60 SECOND ST BLDG 5 PO BOX 855 SHALIMAR FL 32579-0855		

REPORT DOCUMENTATION PAGE

*Form Approved
OMB No. 0704-0188*

Public reporting burden for this collection of information is estimated to average 1 hour per response, including the time for reviewing instructions, searching existing data sources, gathering and maintaining the data needed, and completing and reviewing the collection of information. Send comments regarding this burden estimate or any other aspect of this collection of information, including suggestions for reducing this burden, to Washington Headquarters Services, Directorate for Information Operations and Reports, 1215 Jefferson Davis Highway, Suite 1204, Arlington, VA 22202-4302, and to the Office of Management and Budget, Paperwork Reduction Project(0704-0188), Washington, DC 20503.

1. AGENCY USE ONLY (Leave blank)			2. REPORT DATE	3. REPORT TYPE AND DATES COVERED	
			March 1998	Final, September 1995 - June 1997	
4. TITLE AND SUBTITLE			5. FUNDING NUMBERS		
Determination of the Yield Strength of a Molybdenum Jet			1L162618AH80		
6. AUTHOR(S)					
Miles L. Lampson and Richard L. Summers					
7. PERFORMING ORGANIZATION NAME(S) AND ADDRESS(ES)			8. PERFORMING ORGANIZATION REPORT NUMBER		
U.S. Army Research Laboratory ATTN: AMSRL-WM-TC Aberdeen Proving Ground, MD 21005-5066			ARL-TR-1639		
9. SPONSORING/MONITORING AGENCY NAMES(S) AND ADDRESS(ES)			10. SPONSORING/MONITORING AGENCY REPORT NUMBER		
11. SUPPLEMENTARY NOTES					
12a. DISTRIBUTION/AVAILABILITY STATEMENT			12b. DISTRIBUTION CODE		
Approved for public release; distribution is unlimited.					
13. ABSTRACT (Maximum 200 words)					
The strength of the metal in a shaped charge jet influences its length at breakup, its penetration rate into a target, and its ability to resist aerodynamic forces in flight. The response of a jet to an imposed centrifugal force can be used to estimate its yield strength. Copper was the first metal studied by this technique, and the strength determined by Karpp using a hoop model was approximately 100 MPa. We have studied molybdenum using the same experimental technique and analyzed the data using a hoop, a disk, and a cylinder model of the jet. The yield strength and its associated uncertainty were estimated from the observed kinematics of the portion of the jet fragmented by the centrifugal force and the computed jet spin rate.					
14. SUBJECT TERMS			15. NUMBER OF PAGES		
shaped charge, molybdenum jet strength, yield strength			72		
			16. PRICE CODE		
17. SECURITY CLASSIFICATION OF REPORT		18. SECURITY CLASSIFICATION OF THIS PAGE		19. SECURITY CLASSIFICATION OF ABSTRACT	
UNCLASSIFIED		UNCLASSIFIED		UNCLASSIFIED	
20. LIMITATION OF ABSTRACT					
UL					

INTENTIONALLY LEFT BLANK.

USER EVALUATION SHEET/CHANGE OF ADDRESS

This Laboratory undertakes a continuing effort to improve the quality of the reports it publishes. Your comments/answers to the items/questions below will aid us in our efforts.

1. ARL Report Number/Author ARL-TR-1639 (Lampson) Date of Report March 1998

2. Date Report Received _____

3. Does this report satisfy a need? (Comment on purpose, related project, or other area of interest for which the report will be used.)

4. Specifically, how is the report being used? (Information source, design data, procedure, source of ideas, etc.)

5. Has the information in this report led to any quantitative savings as far as man-hours or dollars saved, operating costs avoided, or efficiencies achieved, etc? If so, please elaborate.

6. General Comments. What do you think should be changed to improve future reports? (Indicate changes to organization, technical content, format, etc.)

Organization _____

CURRENT
ADDRESS

Name _____ E-mail Name _____

Street or P.O. Box No. _____

City, State, Zip Code _____

7. If indicating a Change of Address or Address Correction, please provide the Current or Correct address above and the Old or Incorrect address below.

Organization _____

OLD
ADDRESS

Name _____

Street or P.O. Box No. _____

City, State, Zip Code _____

(Remove this sheet, fold as indicated, tape closed, and mail.)
(DO NOT STAPLE)